

Extraction of crystal-poor rhyolite from a hornblende-bearing intermediate mush: a case study of the caldera-forming Matahina eruption, Okataina volcanic complex

C. D. Deering · J. W. Cole · T. A. Vogel

Received: 10 August 2009 / Accepted: 6 April 2010 / Published online: 29 April 2010
© Springer-Verlag 2010

Abstract The Matahina Ignimbrite (~160 km³ rhyolite magma, 330 ka) was deposited during a caldera-forming eruption from the Okataina Volcanic Centre, Taupo Volcanic Zone (TVZ), New Zealand. Juvenile clasts are divided into three groups: Group (1) the dominant crystal-poor rhyolite type, Group (2) a minor coarse-grained, mingled/mixed intermediate type, and Group (3) a rare fine-grained basalt. The ignimbrite consists of the Group 1 type and is divided into three members: a lower and middle member, which is high-silica, crystal-poor (<10 vol.%) rhyolite, and the upper member, which is low-silica and slightly more crystal-rich (up to 21 vol.%). Cognate, crystal-rich (up to 50 vol.%) basalt to intermediate pumice occurs on top of lag breccias and within lithic-rich pyroclastic density current deposits along the caldera margin (Groups 2 and 3). Several lines of evidence indicate that the intermediate clasts represent the cumulate complement to the melt-rich rhyolite: (1) continuity in the compositions of plagioclase,

orthopyroxene, hornblende, and oxides and normal zoning of individual phenocrysts; (2) the silicic glass from the intermediate magma (interstitial melt) overlaps compositionally with the bulk rock rhyolite and glass; (3) high Zr and a slight positive Eu anomaly in the intermediate magma relative to quenched enclaves from other intermediate TVZ eruptions indicates zircon and plagioclase accumulation, respectively; (4) an increase in the Cl contents in glass from the least evolved to most evolved is consistent with the concentration of volatiles during magma evolution. Most of the compositional variations in the low- to high-silica rhyolites can be accounted for by continued Rayleigh fractionation (up to 15%), following melt extraction from the underlying mush, under varying fO_2 - fH_2O conditions to form a slightly compositionally zoned rhyolitic cap. This link to the varying fO_2 - fH_2O conditions is evidenced by the strong correlation between key geochemical parameters (e.g. Dy, Y), that qualitatively reflect fH_2O conditions (presence or absence of hornblende/biotite), and fO_2 estimated from Fe-Ti oxide equilibrium. Magma mingling/mixing between the basalt-andesite and the main slightly compositionally zoned rhyolitic magma occurred during caldera-collapse, modifying the least-evolved rhyolite at the lower portion of the reservoir and effectively destroying any pre-eruptive gradients.

Communicated by G. Moore.

Electronic supplementary material The online version of this article (doi:10.1007/s00410-010-0524-0) contains supplementary material, which is available to authorized users.

C. D. Deering · J. W. Cole
Department of Geological Sciences, University of Canterbury,
PB 4800, Christchurch 8140, New Zealand

T. A. Vogel
Department of Geological Sciences, Michigan State University,
206 Natural Sciences Bldg., East Lansing, MI 48824-1115, USA

C. D. Deering (✉)
Department of Earth and Space Sciences,
University of Washington, Mailstop 351310,
Seattle, WA 98195-1310, USA
e-mail: cdeering@u.washington.edu

Keywords Taupo Volcanic Zone · Okataina · Matahina eruption · Rhyolite · Andesite crystal-mush

Introduction

Determining the processes governing the generation and maintenance of silicic magma reservoirs is an important area of research in igneous petrology. Variations of two

end-member processes are typically presented: (1) partial melting of crust (Clemens and Wall 1984; Pichavant et al. 1988a, b; Riley et al. 2001; Smith et al. 2003) or (2) crystal fractionation of a mafic progenitor (Bacon and Druitt 1988; Hildreth et al. 1991; Hildreth and Fierstein 2000; Clemens 2003). However, recent numerical models (Dufek and Bergantz 2005) emphasize the difficulty in generating significant volumes of hydrous magma by partially melting the crust. Several variations of the crystal fractionation models have been proposed that invoke the development of an intermediate (andesite–dacite) crystal mush zone (up to 60 vol.% crystals), where crystal-poor, silicic interstitial melt is periodically removed and stored in the upper crust (e.g. Bacon and Druitt 1988; Sisson and Bacon 1999; Hildreth and Fierstein 2000; Bachmann and Bergantz 2004). However, the characteristics, development, and maintenance of such a reservoir or reticulated magma zone capable of producing large volumes of rhyolite still remain unresolved.

These petrogenetic models have also been tested in the Taupo Volcanic Zone (TVZ), New Zealand, over the last several decades. Available geochemical evidence (trace elements, stable and radiogenic isotopes) has been used to suggest that the rhyolites are indeed more likely generated by crystal fractionation of a mafic progenitor in the lower-middle crust accompanied by some degree of assimilation of continental crust (Graham et al. 1992; McCulloch et al. 1994; Graham et al. 1995; Deering et al. 2008). Despite the evidence that these systems may have evolved dominantly by crystal fractionation in New Zealand, a potential mafic progenitor (crystal mush) rarely appears at the surface, either as a primary erupted magma or co-magmatic/eruptive with a rhyolitic magma. For example, evacuation of $\sim 530 \text{ km}^3$ of rhyolitic magma during the 26.5 ka Oruanui eruption included both tholeiitic and calc-alkaline mantle-derived mafic magmas, but these were fine-grained and crystal-poor representing late-stage interaction with the main rhyolitic magma body (Wilson et al. 2006). Several detailed studies of smaller TVZ rhyolitic eruptions ($<150 \text{ km}^3$) have revealed the presence of slight compositional gradients within rhyolitic magma reservoirs prior to eruption (e.g. Milner et al. 2001; Beresford 1997). Alternately, Brown et al. (1998) demonstrated that the voluminous ($\sim 2,000 \text{ km}^3$ of magma, $\sim 340\text{--}320 \text{ ka}$) Whakamaru eruption, although consisting of several rhyolitic compositions that could be related by fractional crystallization, was probably comprised of physically separate magma bodies that had individual evolving histories. Co-magmatic mafic components from each of these eruptions were also typically crystal-poor and apparently interacted with the main rhyolitic magma reservoir during eruption. Hence, the preservation of evidence in eruptive materials of a highly crystalline

cumulate is rare, implying that it either (1) resides physically separate from the main rhyolitic magma reservoir or (2) the magma rheology, incomplete evacuation of the magma reservoir, and/or accompanying caldera-collapse hinders the exhumation of significant amounts of this magma.

This paper documents the petrology and geochemistry of the $\sim 330 \text{ ka}$ Matahina eruption based on an extensive representative sample suite of juvenile rhyolitic and subordinate crystal-rich mafic components. We include an evaluation of the pre-Matahina eruptive products, collectively termed the Murupara subgroup, which consists of eight units of tephra deposits extending back to the Whakamaru eruption $\sim 340 \text{ ka}$, and two pre-caldera lava domes. However, our focus on pre-Matahina eruptions is restricted to the three tephra units that immediately precede the Matahina eruption, which share mineral and compositional characteristics with the Matahina deposits. Our model for the eruption of the Matahina *sensu stricto* provides insight into the development of a large ($>160 \text{ km}^3$ of magma), slightly compositionally zoned crystal-poor rhyolite, which was extracted from a mid- to upper-crustal intermediate mush column.

Regional geologic background

The TVZ in the North Island of New Zealand is a rifted arc (Wilson et al. 1995) and can be divided into segments of dominantly andesitic cone-forming volcanism in the north and south, and a central region characterized by bi-modal volcanism consisting of dominantly rhyolitic caldera-forming and dome-building eruptions and small monogenetic basaltic cinder cones (Healy 1962; Wilson et al. 1984; Fig. 1). Since the inception of volcanism in this central region, 1.6 Ma, $>6,000 \text{ km}^3$ of rhyolitic magma has erupted from eight major eruptive centers. The Okataina Volcanic Centre (OVC), located at the northern extent of the TVZ (Fig. 1), is defined as a complex of coalescing collapse structures, which formed during numerous pyroclastic eruptions over $>400 \text{ kyrs}$. (Nairn 2002), with a total eruptive volume of $>600 \text{ km}^3$ of rhyolite (Cole et al. 2010).

Murupara subgroup

The Murupara subgroup (A–H) consists of a series of tephra deposits found throughout the eastern Bay of Plenty (Manning 1996). The Murupara subgroup includes the Bonisch pyroclastics (Nairn 2002), an obsidian-rich tephra, and the Matahina tephra from the OVC. In the eastern Bay of Plenty, these deposits are found up to 5 meters thick but are dominantly made up of the uppermost, Matahina, eruptive unit.

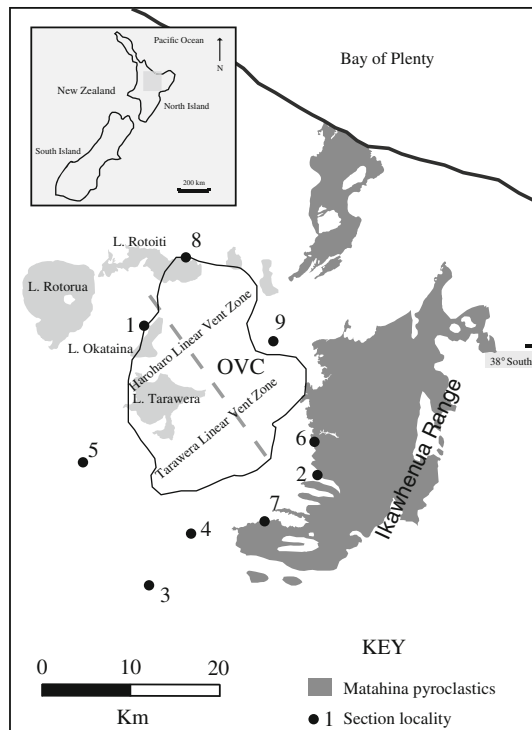


Fig. 1 The central Taupo Volcanic Zone and Okataina Volcanic Centre (OVC) as one of seven major caldera-forming volcanic complexes. Inferred caldera boundaries are outlined in *bold*. Mapped extent of the Matakina outflow sheet *sensu stricto* surrounding OVC and specific sampling localities discussed in the text. Mapped Matakina outflow after Leonard and Beggs (personal communication). *Dashed line* represents traverse for crustal cross-section referred to in discussion

The age of the Murupara subgroup, estimated by Manning et al. (1996) using paleoclimatic data, is between 340 and 330 ka. The final deposit in this sequence, the Matakina (Murupara-H), was formed by a ca. 30 km³ plinian style eruption followed by the voluminous expulsion of greater than 160 km³ of rhyolitic magma during a catastrophic, caldera-forming event (Bailey and Carr 1994; Manning 1995). The Matakina ignimbrite lies mainly to the northeast, east, and southeast, extending radially up to 30 km from the caldera margin (Fig. 1; Bailey and Carr 1994). Bailey and Carr (1994) separated the ignimbrite sequence into three cooling units termed the lower, middle, and upper members that represent three eruptive pulses estimated to have occurred over 20–60 days. These sub-cooling units are recognized in the field by variations in the welding, and specifically, the upper member by a pinkish vapor-phase altered color; presence of clinopyroxene, orthopyroxene, and hornblende; and denser more angular pumice (Bailey and Carr 1994). Lag breccias are found within the upper member capped by pyroclastic density current (PDC) deposits. A single lithic-rich deposit found along the shores of Lake Okataina contains recycled Matakina ignimbrite clasts, lies stratigraphically below

post-Matakina tephra deposits, and contains large (<25 cm) pumice (some amphibole-rich) and lithic clasts consistent with an OVC source. The presence of recycled Matakina ignimbrite clasts in this flow unit and its stratigraphic position below a thick post-Matakina plinian fall deposit indicate that this flow was likely emplaced contemporaneously with the Matakina upper member.

Sampling and analytical techniques

Pumice, fiamme, ignimbrite clasts, rhyolite lava, and rhyolite lithics were sampled from the upper Murupara subgroup pyroclastic fall and flow deposits (Units E–H) in an attempt to best represent the full distribution of the OVC volcanic activity leading up to and including the Matakina eruption. Fiamme were cut out of welded ignimbrite and trimmed to remove the attached matrix. Small (<2 cm) pumice clasts were removed from ‘recycled’ Matakina-type ignimbrite clasts from within the Matakina outflow sheet. The most abundant rhyolite lithics found in the Matakina plinian fall deposit and lag breccias were sampled for analysis to explore their relationship to the Matakina magma(s).

Dense basalt–dacite pumice clasts were found at two localities: (1) along the western caldera margin (Fig. 1; locality 1) within the lithic-rich pyroclastic flow deposit and (2) directly above a lag breccia within a PDC deposit east of the caldera margin (Fig. 1; locality 2). A total of 200 representative samples were analyzed by X-ray fluorescence (XRF) and laser ablation inductively coupled mass spectrometry (LA-ICP-MS).

Samples were trimmed using a diamond grinder and saw to remove any weathered rind or organic matter. Sample fragments were then cleaned in a sonic bath of distilled water for 10 min to remove any surface contaminants from the grinder and saw, then placed in an oven at 100°C for a minimum of 24 h. These dry fragments were rough crushed using a tungsten carbide, pneumatic press. Any additional weathered fragments were removed from the sample aggregate prior to milling in a Frisch Planetary agate mill.

For the XRF and LA-ICP-MS analyses, three grams of the milled rock powder and 9.0 g of lithium tetraborate (Li₂B₄O₇), along with 0.5 g of ammonium nitrate (NH₄NO₃; used as an oxidizer), were fused in platinum crucibles at 1,000°C for 20–30 min on an orbital mixing stage. The melt was then poured into platinum molds, making a glass disk that was analyzed using a Bruker S-4 X-ray fluorescent (XRF) spectrometer. XRF major element analyses were reduced by a fundamental parameter data reduction method using Bruker Spectra Plus[®] software, while XRF trace-element (Rb, Sr, and Zr) data were calculated using standard linear regression techniques using the ratio of the element peak to the Rh Compton peak, which corrects for mass

absorption. Prior to any calculations, the background signal was subtracted from the standards and samples. Major- and trace-element concentrations in the samples were calculated based on a linear regression method using BHVO, W-2, STM-1, MRG-1, SY-2, SY-3, DNC-1, PCC-1, JA-2, JA-3, BIR, QLO-1, and RGM-1 standards.

The rare-earth elements and Nb, Ta, Hf, Ba, Y, Th, U, and Pb were determined by LA-ICP-MS on the same glass disks as used for XRF analyses. A Cetac LSX200 + laser ablation system was used, coupled with a Micromass Platform ICP-MS, using strontium determined by XRF as an internal standard. Trace-element data reduction was done using MassLynx software. Element concentrations in the samples were calculated based on a linear regression method using well-characterized standards. All major- and trace-element whole rock analyses reported here were conducted at Michigan State University. Precision and accuracy of both XRF and LA-ICP-MS chemical analyses are reported in Vogel et al. (2006).

Mineral and glass compositions were determined using a Cameca SX 100 EPMA equipped with five wavelength spectrometers at the University of Michigan. For the minerals, we used an accelerating potential of 15 kV, a focused beam with a <1- μm spot size, counting time of ~ 3 min/mineral, and a 10-nA beam current. The beam spot size was increased to 10 μm and beam current reduced to 4 nA for glass analyses to reduce Na loss. Standards used were natural fluor-topaz (FTOP); natural jadeite (JD-1); natural grossular, Quebec (GROS); natural adularia, St. Gothard, Switzerland (GKFS); synthetic apatite (BACL); synthetic Cr_2O_3 ; and synthetic FeSiO_3 (FESI).

$^{87}\text{Sr}/^{86}\text{Sr}$ and $^{143}\text{Nd}/^{144}\text{Nd}$ isotope ratios were measured by multi-collector inductively coupled plasma mass spectrometry (MC-ICPMS) at Victoria University of Wellington. Samples for Sr isotopic analysis were digested using Hf- HNO_3 techniques and Sr separated using Sr-spec Eichrom resin. Sr mass spectrometric techniques used are a modified version of those described in detail by Waight et al. (2002). Samples for Nd isotopic analysis were digested using flux-fusion techniques (Ulfbeck et al. 2003) and Nd separated using conventional cation exchange and Ln-spec Eichrom resins. Isotopic ratios were corrected for instrumental mass bias using the exponential law ($^{86}\text{Sr}/^{88}\text{Sr} = 0.1994$; $^{146}\text{Nd}/^{144}\text{Nd} = 0.7219$) and normalized to $^{87}\text{Sr}/^{86}\text{Sr} = 0.710248$ (SRM987) and $^{143}\text{Nd}/^{144}\text{Nd} = 0.5128980$ (BHVO-2). External reproducibility of $^{87}\text{Sr}/^{86}\text{Sr}$ and $^{143}\text{Nd}/^{144}\text{Nd}$ ratios is better than ± 0.00002 .

Petrography

Phenocryst contents were determined by point counting on thin sections of selected samples or by least-squares mass

balance using bulk rock, glass, and mineral chemistry (Tables 1, 2). We have divided the rocks into three main groups on the basis of their mineral assemblages and bulk geochemistry. The dominant suite (Group 1) constitutes the most voluminous component of the eruption, the rhyolite, and was further divided into three subgroups (Groups 1a, 1b, 1c). The subordinate Group 2 ranges in composition from andesite to dacite and typically shows obvious evidence of mingling/mixing in hand sample and thin section. Group 3 are rare, fine-grained basaltic lapilli.

Rhyolitic rocks (Group 1)

The Matahina Group 1 rhyolite pumice and lithics have crystal contents ranging from 3 to 21% (Table 1). Samples within Group 1a, 1b, and 1c each have distinct mineral assemblages: (1a) crystal-poor (<5%), containing quartz + plagioclase + magnetite + orthopyroxene \pm hornblende + ilmenite; (1b) crystal-poor/moderate (5–21%), containing plagioclase + quartz + hornblende + orthopyroxene + magnetite + ilmenite \pm biotite; and (1c) crystal-poor/moderate (4–17%), containing quartz + plagioclase + biotite + magnetite + ilmenite. Accessory zircon, apatite, and pyrrhotite are present as microphenocrysts and mineral inclusions.

Plagioclase is the dominant felsic mineral in Group 1a,b, but is generally less abundant than quartz in Group 1c. Phenocrysts are subhedral to euhedral and typically <2 mm with subtle zoning. Quartz is subhedral to euhedral, and up to 2 mm in Group 1a and 6 mm in Group 1c. The quartz/plagioclase ratio increases with increasing SiO_2 in Group 1a (Table 1). In contrast, Group 1c always has high quartz/plagioclase ratios compared to Group 1a,b with no apparent relationship to bulk-rock SiO_2 wt. %. Hornblende in the high-silica Group 1a,b are subhedral to euhedral and almost exclusively elongate and bladed up to 1 mm. Crystal habits are more varied in the low-silica, Group 1b, including blocky and tabular euhedral types up to 1.5 mm, in addition to the bladed type. The abundance of hornblende is inversely proportional to total crystallinity and bulk rock SiO_2 wt% in the Group 1b from the Matahina *sensu stricto* and is rarely present in the Group 1a (

Table 1). Orthopyroxene are subhedral to euhedral and up to 1 mm in the Group 1b, although mostly <0.5 mm. Clinopyroxene are rare and only found in the Group 1b pumice. Biotite is dominantly found in the Group 1c rhyolite as flakes and books up to 1.2 mm. In contrast, the rare biotite in Group 1b clasts are flakes <0.5 mm in length. Magnetite and ilmenite are ubiquitous in the Matahina rhyolite pumice and are typically found included in orthopyroxene and less commonly in hornblende. Magnetite also occur as individual phenocrysts and are anhedral to euhedral up to 0.4 mm. Exsolution lamellae were identified in magnetite from all groups.

Table 1 Phenocryst assemblages observed in selected Matahina juvenile pumice clasts and rhyolite lava lithics

Sample	Group	Map	Deposit	Bulk rock SiO ₂ (wt. %)	Glass	Plag	Hb	Oxides/ Mgt	Ilm	Opx	Biot	Qtz	Qtz/ Plag	Hb/ Opx	Phenocryst total	$\sum r^2$
UC175	1b	3	Ash-flow	72.68	0.79	0.167	0.001	0.013	0.003	0.027	–	–			21.0	0.08
						79.5	0.3	6.0	1.3	12.9	–	–	0.02			
UC168	1b	4	Ash-flow	75.17	0.89	0.068	0.009	0.004	0.002	0.011	–	0.016			11.0	0.15
						61.5	7.9	3.9	2.2	9.6	–	14.9	0.2	0.8		
UC649	1b	5	Ash-flow	76.94	0.95	0.015	0.006	0.005	0.0001	0.001	–	0.024			5.0	0.02
						29.9	12.1	9.1	0.4	1.1	–	47.5	1.6	11.0		
UC842	1a	6	Plinian	75.84	96.9	1.0	–	0.2		0.1	–	2.0			3.1	
						30.2	–	4.8		1.6	–	63.5	2.1			
UC887	1a	7	Plinian	77.85	96.7	1.1	–	0.1		0.1	–	2.2			3.3	
						31.8	–	1.5		1.5	–	65.2	2.0			
UC813	1b	1	PDC	72.80	91.6	6.2	1.5	0.4		0.4					8.4	
						73.2	17.3	4.8		4.8				3.6		
UC498	1b	2	PDC	71.16	94.4	3.2	1.4	0.3		0.4		0.4	0.1		5.7	
						55.8	24.8	5.3		7.1		7.1		3.5		
UC812	1a	1	PDC													
UC811	1b	1	PDC	72.63	80.9	5.7	0.2	0.3		1.0	0.8	11.3			19.2	
						29.8	0.8	1.3		5.0	4.2	59.0	2.0	0.2		
UC892	1c (lithic)	2	Lag breccia	77.48	0.96	0.001	–	0.001	0.000	–	0.017	0.023			4.0	0.01
						2.0	–	1.6	0.2	–	40.6	55.6	27.8			
UC1091	1c (lithic)	4	Plinian	77.58	92.5	3.2	–	0.1		–	0.7	3.6			7.5	
						42.0	–	1.3		–	9.3	47.3	1.1			
UC853	1a (lithic)	6	Plinian													

Modal phenocryst abundances were determined by counting 2,000 pts. per thin section or calculated by least-squares methods using glass, phenocryst, and bulk-rock compositions. Map refers to localities in Fig. 1. *PDC* pyroclastic density current

Table 2 Phenocryst assemblages observed in selected Matahina juvenile basalt–dacite clasts

Sample	Group	Map	SiO ₂ (wt. %)	G' mass	Plag	Amph	Oxides	Opx	Cpx	Qtz	Phenocryst total
UC839	3	2	51.29	57.4	0.1	38.3	4.1	0.1	–	–	42.6
					0.2	89.9	9.6	0.2	–	–	
UC816	2	1	56.79*	73.0	11.0	11.8	2.0	1.9	0.3	–	27.0
					40.7	43.7	7.4	7.0	1.1	–	
UC1100	2	1	57.65	51.8	28.0	16.9	1.6	1.1	0.6	0.1	48.2
					58.1	35.0	3.3	2.2	1.3	0.05	
UC1123	2	1	63.75	76.9	13.2	5.9	1.1	2.7	0.2	0.1	23.1
					57.0	25.4	4.8	11.8	0.9	0.05	
UC520	2	2	58.66	72.2	18.2	4.9	2.0	2.4	0.2	–	27.8
					65.6	17.8	7.2	8.7	0.7	–	
UC832	2	2	66.33	83.7	9.8	4.1	0.3	1.8	0.1	0.2	16.3
					60.1	25.2	1.8	11.0	0.6	1.2	

Modal abundances acquired by counting 1000 pts. per thin section. * SiO₂ determined by mass balance using glass and phenocryst compositions. Map refers to localities in Fig. 1

Mingled/mixed intermediate rocks (Group 2)

Group 2 intermediate rocks are porphyritic with crystal contents ranging from 16 to 49 vol.% and crystal contents

decrease from andesite to dacite (Table 2). A distinct clast type is the least-evolved basaltic–andesite clast (bulk composition determined by mass balance using glass and phenocryst compositions), which shows obvious signs of

distinct glasses in hand sample and has a lower crystallinity than the andesite. Although varying in abundance, the mineral assemblage for Group 2 is plagioclase + amphibole + orthopyroxene ± clinopyroxene + magnetite + ilmenite + zircon + apatite ± quartz.

Textures such as glomerocrysts, embayed plagioclase, and corroded plagioclase with overgrowths are common features in the mafic clasts (Fig. 2). Glomerocrysts include all phases in the assemblage, but those with adcumulate textures (sutured grain boundaries) are typically dominated by hornblende, although a few are orthopyroxene dominated and are up to 2.5 mm in diameter. Amphibole is anhedral within some of the glomerocrysts as a function of the adcumulate texture, but are more commonly intergrown with oxides and plagioclase and are euhedral up to 3 mm. Clinopyroxene is anhedral and commonly enclosed within large (2 mm) hornblende phenocrysts but also occurs as subhedral individual phenocrysts (<2.0 mm). Most plagioclase (up to 3.5 mm) displays deep embayments, with almost skeletal surfaces where melt has infiltrated into the center of the grain (Fig. 2). Although not seen on all of the large, near skeletal, plagioclase, overgrowths occur and range in width from ~50 to 150 μm. Orthopyroxene is subhedral to euhedral phenocrysts up to 1.8 mm in length. Oxides are anhedral to euhedral up to 0.4 mm. Quartz is subhedral to euhedral, bipyramidal, and up to 0.5 mm in length. Zircon and apatite are typically found included in amphibole and pyroxene and occur as euhedral crystals up to 150 μm.

Basalt (Group 3)

Rare basaltic clasts are fine-grained, hornblende-rich (up to 90% modal), and crystal-rich (~43 vol.%). The complete mineral assemblage is hornblende + plagioclase + oxides. Plagioclase crystals commonly occur as microlites, but are sometimes larger (up to 3.0 mm) than the more abundant hornblende and oxides and have corroded cores and thin overgrowths (<50 μm; Fig. 2c). Most hornblende are small, subhedral to euhedral, but the sparse larger crystals are either acicular or have small orthopyroxene with pseudomorphed hornblende overgrowths.

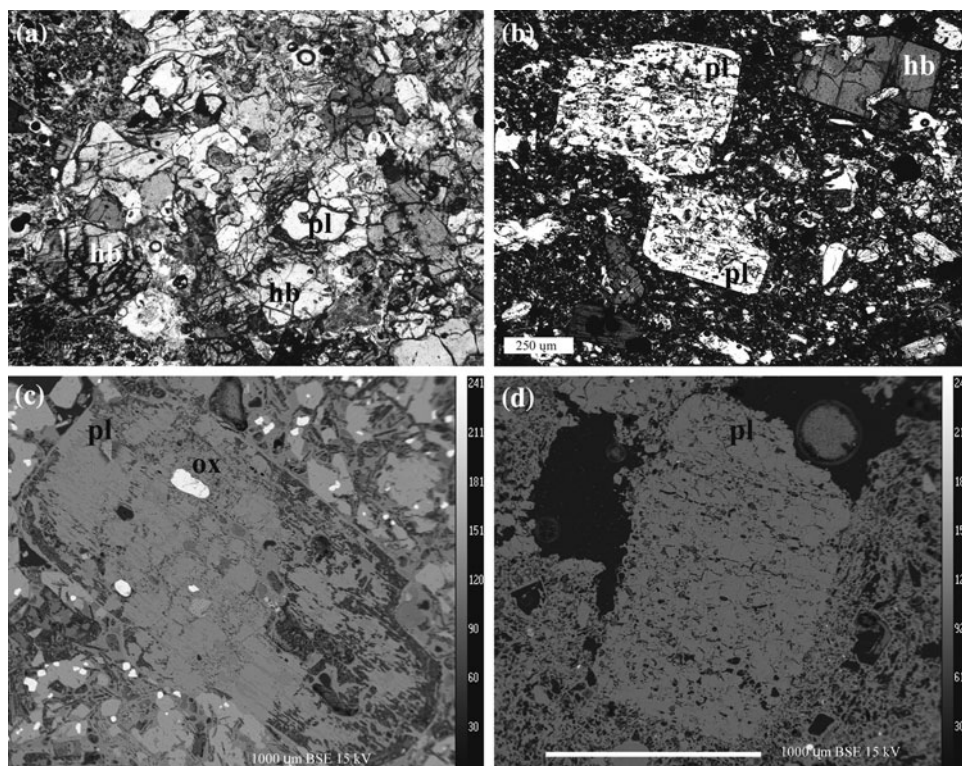
Mineral chemistry

Core and rim compositions of phenocrysts representing Groups 1–3 were analyzed. Group 1 samples were selected to reflect the range of SiO₂ contents from Murupara tephrastratigraphy (E–H), and the full distribution of the Matahina outflow sheet (Fig. 1). The complete dataset of mineral chemistry is available in Electronic Appendix 1.

Plagioclase

Plagioclase in Group 1 ranges in composition from An₅₃ to An₂₁ and Or_{4.5} to Or_{0.8} (Fig. 3a). The highest Or contents are observed in Group 1c and form a slightly divergent

Fig. 2 Photomicrographs of **a** typical glomerocrysts of sutured hornblende and plagioclase in andesite to dacite clasts and **b** embayed and dissolved plagioclase. *Backscattered* images of **c** large corroded plagioclase with thin overgrowth and **d** typical, deeply corroded and dissolved plagioclase similar to that displayed in **(b)**. Pl = plagioclase; hb = hornblende; ox = Fe–Ti oxide



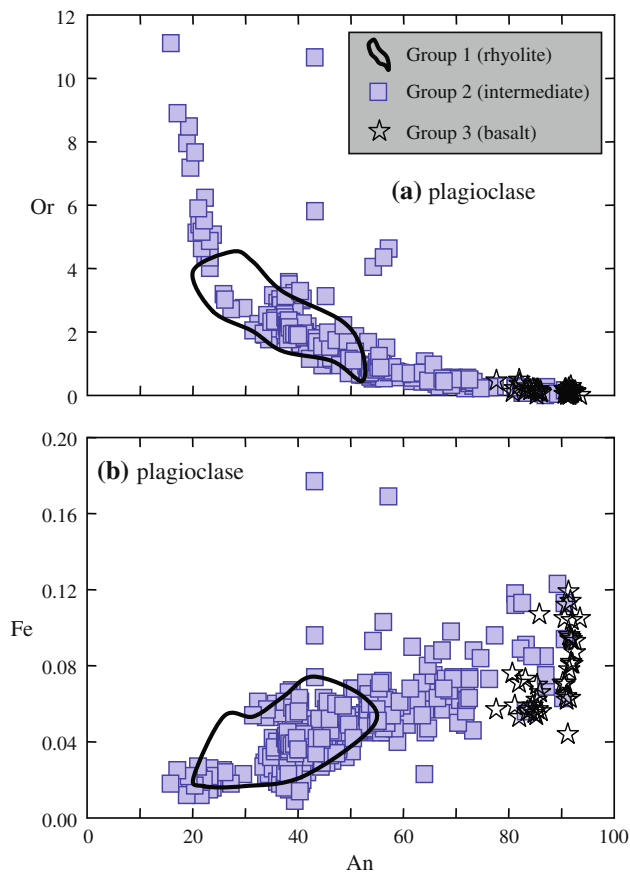


Fig. 3 Or and Fe against An in plagioclase for basalt to high-silica rhyolite

trend from Group 1a,b plagioclase. The Fe content increases with An content and decreases with K content (Fig. 3). Groups 1a and 1c plagioclase are generally the lowest An % and Group 1b the highest. Most individual grains are unzoned or slightly normally zoned, but those found in the upper deposit with the mafic clasts show reverse zoning. Rare sanidine is found in Group 1c but appears only as microlites (<50 μm).

Plagioclase compositions in Groups 2 and 3 form a continuous range from An_{15} to An_{94} and $\text{Or}_{0.01}$ to Or_{11} (Fig. 3a). Similar to Group 1, Fe is positively correlated with An content (Fig. 3b) and negatively correlated with K. Intermediate pumice compositions have a wide range of An, but the plagioclase with the highest An content are the largest subhedral crystals found in the Group 3 basalt (up to An_{94} ; Fig. 3a). Individual grains show both reverse and normal zoning, but the crystal population appears very diverse with many that are nearly unzoned.

Amphibole

Amphibole in Group 1 are calcic and tschermakite to magnesiohornblende, using the classification of Leake

et al. (1997). Al_{IV} contents correlate well with Ti, $(\text{Na} + \text{K})_{\text{A}}$, and Ca (e.g. Fig. 4a). The Cl contents are well correlated with K and most other elements (e.g. Fig. 4b).

In Groups 2 and 3, calcic amphibole are classified as Ti-magnesiohastingsite, magnesiohastingsite, Ti-tschermakite, tschermakite, magnesiohornblende, and cummingtonite. Cummingtonite occurs as hornblende overgrowths and as smaller individual groundmass phenocrysts in a few clasts. Al_{IV} contents correlate well with Ti ($\text{Na} + \text{K})_{\text{A}}$, and Ca (e.g. Fig. 4a). Although the compositions of the hornblende generally overlap, it is important to note that the high Ti population in the rhyolite are from the upper ignimbrite member and most of the rhyolite hornblende cluster at the low Ti end. Similarly, the rhyolite hornblende is dominantly clustered at higher Cl and K contents than the Groups 2 and 3 hornblende, although overlapping (Fig. 4b).

Biotite

Biotite from Group 1c rhyolite lithics and juvenile pumice clasts from the PDC deposit along the western caldera margin (Fig. 1; locality 1) are similar in composition (Fig. 4c,d). However, those pumice that also contain orthopyroxene and amphibole, also include a population with much higher MgO (Fig. 4c). Biotite from the rhyolite lava lithics have the lowest Cl contents (Fig. 4d).

Orthopyroxene

Group 1 orthopyroxene compositions range between En_{60} and En_{40} and $\text{Wo}_{3.3}$ and $\text{Wo}_{0.9}$. Group 1b orthopyroxene encompass the entire En and Wo range, but are dominantly higher than the Group 1a. Orthopyroxene are generally unzoned in the high-silica rhyolite, but some show normal zoning from $\sim\text{En}_{56}$ to En_{47} in the low-silica rhyolite. Clinopyroxene are rare and only found in the low-silica Group 1b pumice; compositions are $\sim\text{En}_{35}$ and $\sim\text{Wo}_4$.

Group 2 orthopyroxene compositions range between En_{78} and En_{47} and $\text{Wo}_{1.8}$ and $\text{Wo}_{4.0}$. Some crystals are strongly normally zoned from En_{65} to En_{42} or slightly reversely zoned, whereas most analyzed are unzoned. The rare clinopyroxene, which are typically found as inclusions with pseudomorphed hornblende, range from En_{41} to En_{44} and Wo_{42} to Wo_{47} .

Considering the obvious signs of mixing/mingling between the Group 1 rhyolite and Groups 2 and 3 mafics, we have assessed whether or not the pyroxene crystals are in equilibrium with the host melt-rock. The range of distribution coefficients used ($^{Fe/Mg}K_{\text{Dmin/liq}}$: 0.19–0.31) was determined in experiments where low- to high-silica rhyolite melt was in equilibrium with mineral assemblages (plag + hbl + opx + ox) and under conditions (T: 825°C

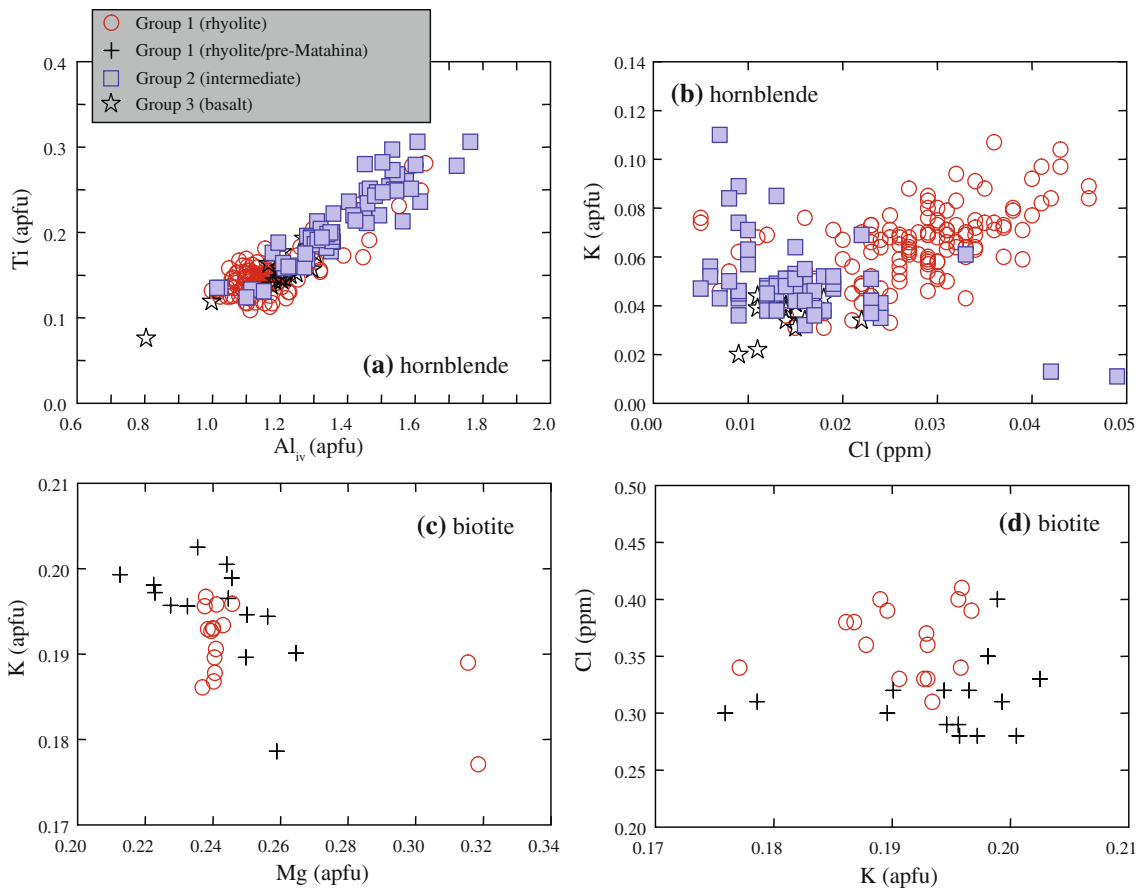


Fig. 4 a–b Hornblende compositions from basalt to high-silica rhyolite. c–d Biotite compositions from Matahina ignimbrite and pre-Matahina rhyolite lava

and fO_2 : near QFM) similar to those estimated for the Matahina rocks (Sisson et al. 2005). Most of the pyroxene analyzed from the Groups 1a and 1b appear to be in equilibrium with the host melt, but a subordinate population of higher Mg# is not (Fig. 5a,b). Pyroxene with the lowest and highest Mg# from Group 2 are in equilibrium with the melt and bulk-rock, respectively; however, the intermediate compositions appear in disequilibrium (Fig. 5c). Most of the compositions from both the Group 1b and Group 2 pyroxene that are in disequilibrium with the melt are crystal cores and would be in equilibrium with the bulk magma and, therefore, can be explained in terms of melt evolution. In contrast, rims out of equilibrium reflect mixing between contrasting melt compositions.

Fe–Ti oxides

The compositional range of magnetite from Groups 1–2 is relatively continuous (e.g. Fig. 6a). However, most Group 2 magnetite analyzed is higher in X_{Mg} compared to Group 1 and only a few fall within the Group 1 field (Fig. 6a). Similar to the magnetite, ilmenite form a continuous

compositional trend within the Group 1 rhyolite. Group 2 have the highest X_{Mg} ilmenite and also overlap with Group 1 (Fig. 6b).

Intensive parameters and water content

Pre-eruptive temperatures and oxygen fugacities were estimated by Fe–Ti oxide equilibrium using the method of Ghiorso and Evans (2008), which has an uncertainty of $\pm 30^\circ\text{C}$ (Fig. 7). Magnetite and ilmenite grains in direct contact were preferred for calculations; however, most were not actually touching but included in single orthopyroxene phenocrysts. Therefore, the equilibrium test of Bacon and Hirschmann (1988) was used to determine the suitability of oxide pairs for temperature-oxygen fugacity estimates. Temperatures of low-silica, Group 1a,b were also estimated by clinopyroxene–orthopyroxene equilibrium using the method of Ghiorso and Sack (1991). Results are given in Table 3.

The average Group 1 pre-eruptive temperature and oxygen fugacity calculated for the high-silica rhyolite

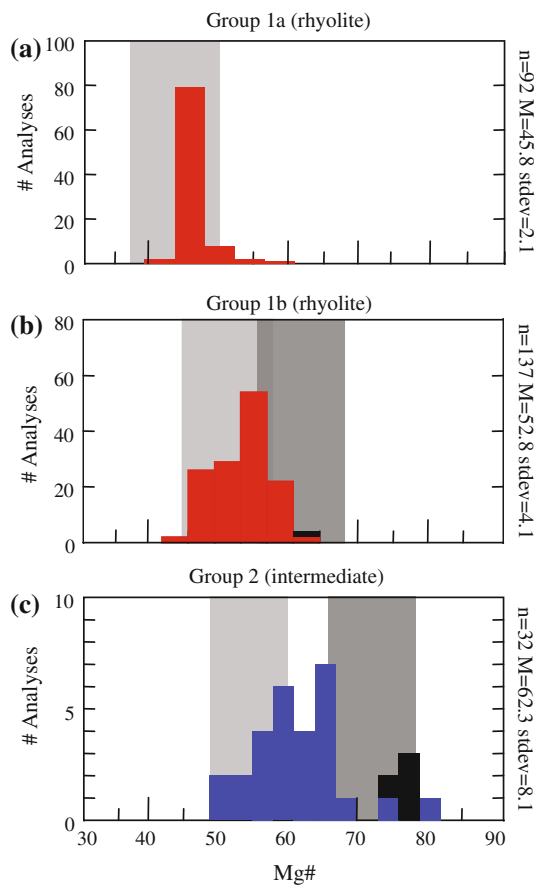


Fig. 5 Histograms showing Mg# of orthopyroxene (Red and Blue) and clinopyroxene (Black) cores and rims from the Matahina rhyolite and mingled/mixed intermediate pumice. Ranges of pyroxene compositions, in equilibrium with the glass and bulk rock compositions, calculated using $^{Fe/Mg}K_{Dmin/liq}$ values between 0.19 and 0.31 (Sisson et al. 2005). An average high-silica rhyolite glass composition was used for Group 1a, average low-silica rhyolite for Group 1b, and the lowest SiO₂ rhyolite glass measured was used for Group 2 (light gray shading). The bulk rock composition of a low-silica rhyolite was used for Group 1b and a dacite for Group 2 (dark gray shading)

compositions is 766°C and log units (ΔNNO ; relative to the nickel-nickel oxide buffer) = -0.12, respectively. The temperature estimated for the low-silica, Group 1b rhyolite is 866°C (log units ΔNNO = 0.18), whereas clinopyroxene–orthopyroxene yields 853°C. These low-silica, Group 1b pumice is only found in the PDC deposit overlying the lag breccia outside of the eastern caldera margin, in ‘upper member’ pyroclastic flow deposits to the east-southeast and southwest of the caldera margin, and within the Lake Okataina biotite-bearing PDC deposit within the western caldera margin (Fig. 1). While the Group 1c Fe–Ti oxide estimates yield temperatures within error of the high-silica Group 1a (778°C), the oxygen fugacity is distinctly higher (log units ΔNNO = 0.50) than either of the Group 1a,b rhyolites.

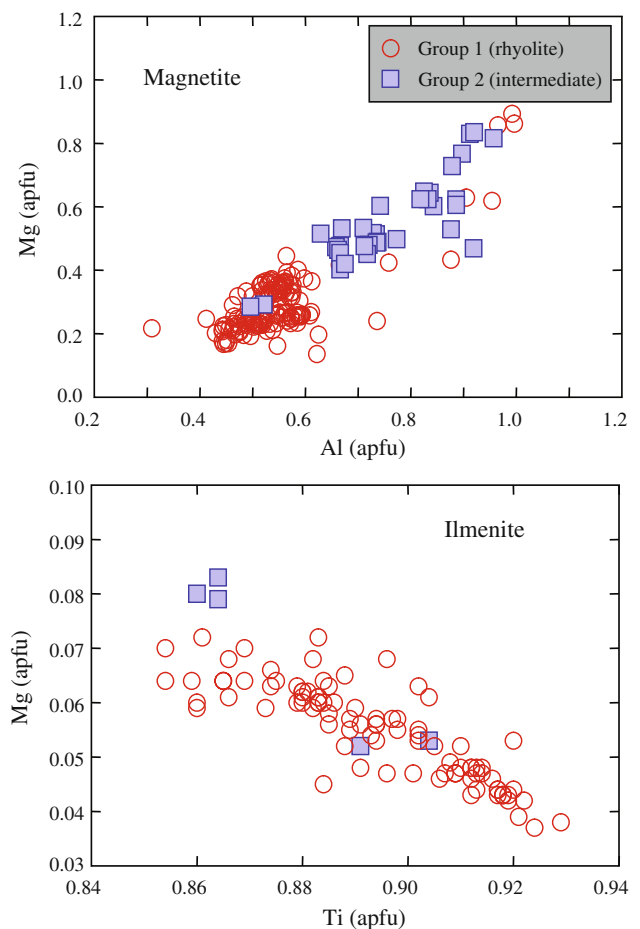


Fig. 6 Composition of oxides in intermediate and silicic rocks

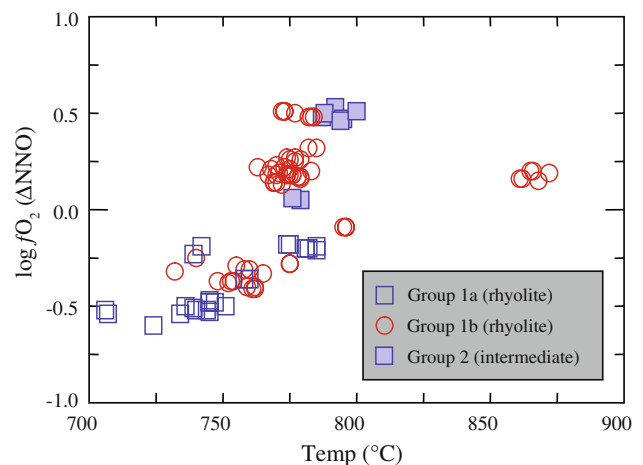


Fig. 7 T- fO_2 determined using Fe–Ti oxide equilibrium pairs for the intermediate to silicic rocks ($n = 109$)

Pressure estimates using Al-hornblende are inherently difficult for volcanic rhyolite compositions from the TVZ as they typically lack the full buffering assemblage that is required (plagioclase + quartz + biotite + sanidine + hornblende + sphene), allowing the composition to change

Table 3 Geothermometry comparison

Method	Ti–hb (°C)	Plag–hb (°C)	Fe–Ti oxide (°C)	Cpx–opx (°C)	fO_2 (Δ NNO)
<i>Rock type (group)</i>					
Low-silica rhyolite (1b)	–	836	866	853	0.18
Rhyolite (1c)	–	748	778	–	0.50
High-silica rhyolite (1b)	–	772	770	–	0.00
High-silica rhyolite (1a)	–	774	758	–	–0.38
<i>Pre-Matahina rhyolite dome</i>	–	–	712	–	–0.55
Fine-grained basalt (3)	727	–	–	–	–
Basaltic–andesite (2)	867c/828r	–	–	953	–
Andesite (2)	831c/760r	–	793	882	0.49
Andesite (2)	810c/765r	–	–	885	–
Dacite (2)	784c/756r	–	778	–	0.06
Dacite (2)	813c/780r	–	–	–	–

Ti–hb: Féménias et al. (2006); Plag–hb: Holland and Blundy (1994); Fe–Ti oxide and oxygen fugacity: Ghiorso and Evans (2008)
 Cpx–opx: Ghiorso and Sack (1991). hb: hornblende; plag: plagioclase; cpx: clinopyroxene; opx: orthopyroxene; r: rim and c: core

freely with temperature and oxygen fugacity. Only the Group 1c pumice has the appropriate phase assemblage (with the exception of sphene), restricting quantitative interpretations of pressure to this group. However, Deering (2009) showed that the Al–Tschermak coupled exchange between Al_{vi} and Al_{iv} in hornblende, which is pressure dependent, accounted for some of the changes in Matahina hornblende composition, concluding that Al–geobarometers (e.g. Schmidt 1992) could provide a relative indication of pressure among rhyolite groups. The results of that study showed that at least a portion of the crystal cargo in the low-silica rhyolite (Group 1b) crystallized at greater depths than the high-silica rhyolite (Group 1a), ~ 300 MPa (10–12 km) and ~ 100 –200 MPa (4–6 km), respectively.

Blundy and Cashman (2001) showed that in silica- and water-saturated melts pressure and temperature could be estimated from glass compositions projected into the synthetic Qz–Ab–Or–H₂O system and for relative pressures from silica-undersaturated melts. Quartz is present in the Matahina rhyolites (although rare in pumice <73 wt. % SiO₂), indicating silica-saturation. Water-saturation has not yet been determined using volatile abundances, but Johannes and Holtz (1990) demonstrated that in water-undersaturated experiments, the cotectics are not significantly different than in water-saturated melts. Glass compositions of Group 1 rhyolites plot between 100 MPa and 300 MPa (4–12 km depth), with the low-silica Group 1b rhyolite at the highest pressures from 200 to 300 MPa (up to 12 km depth). These results are similar to those determined by Al–hornblende geobarometry, indicating that the low-silica rhyolite crystallized at greater depths than the high-silica rhyolite. Although we recognize the limitations of both these methods, we suggest they provide

useful relative estimates of crystallization depths among the different magma groups.

Pre-eruptive temperatures and oxygen fugacity of the basalt (Group 3) and intermediate (Group 2) rocks were estimated using several geothermometers: Fe–Ti oxides equilibrium, clinopyroxene–orthopyroxene, Ti–hornblende. The results of these calculations are summarized in Table 3. Iron–titanium oxide equilibrium calculations yield temperatures for the Group 1c andesite and Group A dacite within error of the eruptive temperatures determined for the Matahina rhyolite ($\sim 785 \pm 30^\circ\text{C}$). Temperatures estimated for basaltic–andesite to andesite hornblende cores, using the Ti–hornblende geothermometer of Féménias et al. (2006), average $\sim 850^\circ\text{C}$, which is within error of those determined by clinopyroxene–orthopyroxene pairs ($\sim 920^\circ\text{C}$). Similar to the temperatures estimated using Fe–Ti oxide equilibria for the andesite to dacite pumice, the hornblende rims yield $\sim 765^\circ\text{C}$. The fine-grained basalt temperature is 727°C , slightly less than the eruptive temperature of the other mafic clasts. Oxygen fugacity in the mafic Group 1c is similar to that estimated for the Group 1c rhyolite and higher than the mafic and felsic Group 1a,b rocks.

Water contents were only estimated for the Group 1 rhyolite using plagioclase rim and glass compositions, assumed to be in equilibrium by the method of Housh and Luhr (1991). Estimates range from 2.77 to 5.42 wt. % H₂O (An method) and 3.61–5.70 wt. % H₂O (Ab method), from the low-silica to high-silica rhyolite types, respectively (samples: UC175, UC649, UC555, UC808). The increase in H₂O contents from low- to high-silica rhyolite types coincides with an increase in the abundance of modal hornblende in Group 1b (Table 2).

Table 4 Representative Matahina basalt to rhyolite bulk geochemical analyses

Sample	UC813	UC498	UC175	UC181	UC168	UC649
Lithology	Matahina	Matahina	Matahina	Matahina	Matahina	Matahina
Group	1b	1b	1b	1b	1b	1b
Deposit description	PDC	PDC	Pinkish tuff	Pinkish tuff	Gray tuff	Pinkish tuff
Type	Dense pumice	Pumice	Pumice	Pumice	Pumice	Pumice
Location	Lk. Okataina	Te Weta Rd.	Reihana Rd.	Reihana Rd.	Pahekeheke Rd.	SH38
Grid reference	U16/079355	V16/300301	U17/092099	U17/092099	V16/356186	V16/113141
SiO ₂	72.80	71.16	72.68	74.58	75.56	76.94
TiO ₂	0.34	0.45	0.37	0.27	0.23	0.19
Al ₂ O ₃	14.75	16.00	14.55	13.60	13.63	12.82
Fe ₂ O ₃	2.67	3.48	2.81	2.26	1.77	1.46
MnO	0.06	0.07	0.06	0.06	0.05	0.04
MgO	0.66	0.86	0.63	0.52	0.41	0.21
CaO	2.22	2.06	2.05	2.07	1.48	1.07
Na ₂ O	3.59	3.07	3.51	3.69	3.57	3.41
K ₂ O	2.89	2.81	3.31	2.92	3.28	3.85
P ₂ O ₅	0.02	0.02	0.02	0.01	0.02	0.01
LOI	3.85	4.26	3.30	4.80	3.22	3.58
Total	96.00	95.61	96.57	95.05	96.65	96.29
V	30.00	66.31	29.21	14.77	12.80	1.31
Cr	4.89	10.63	4.61	3.25	5.23	3.95
Ni	18	18	17	17	17	17
Cu	–	6	3	3	5	1
Zn	45	54	42	41	45	31
Rb	95	89	98	87	105	116
Zr	219	263	254	291	208	156
Sr	181	165	170	180	141	99
Y	20.72	19.78	21.16	24.40	23.87	19.11
Nb	8.60	10.75	8.79	7.76	9.62	8.32
Ba	786	726	686	659	833	839
La	20.60	18.68	19.66	18.98	23.19	21.64
Ce	43.00	49.81	47.76	39.97	49.91	45.87
Pr	4.08	4.10	4.41	4.39	5.57	4.23
Nd	14.13	14.59	15.39	16.11	18.06	14.36
Sm	2.84	3.20	3.05	3.33	3.27	2.92
Eu	0.74	0.92	0.82	0.91	0.80	0.63
Gd	3.00	3.22	3.60	3.80	3.80	3.20
Tb	0.48	0.53	0.55	0.58	0.57	0.50
Dy	2.80	2.92	3.13	3.52	3.24	2.83
Ho	0.52	0.62	0.61	0.71	0.66	0.57
Er	1.77	1.86	1.94	2.18	2.01	1.84
Yb	2.05	2.08	2.19	2.43	2.25	2.01
Lu	0.34	0.32	0.34	0.41	0.37	0.34
Hf	4.97	5.86	5.79	6.36	5.02	3.97
Ta	1.04	1.22	1.42	1.09	2.15	1.65
Pb	21.45	25.34	23.15	22.82	33.15	32.15
Th	12.06	11.45	13.05	9.45	12.90	13.51
U	3.21	3.34	3.10	2.46	3.77	4.21
⁸⁷ Sr/ ⁸⁶ Sr				0.705908		
¹⁴³ Nd/ ¹⁴⁴ Nd						

Geochemistry

Bulk-rock major and trace elements

Juvenile pumice and fiamme, pre-Matahina rhyolite lava, rhyolite lithics, and recycled ignimbrite have been

analyzed to represent the full spectrum of eruptive deposits and magma types. Representative data are provided in Table 4, and the full dataset is available as Electronic Appendix 2.

In general, the Group 1 rhyolite and Group 2 intermediate clasts are calc-alkaline, whereas the Group 3 basalt

Table 4 continued

UC650 Matahina 1b Pinkish tuff Pumice SH38 V16/113141	UC842 Matahina 1a Plinian airfall Pumice Ohakiri Rd. V16/298277	UC887 Matahina 1a Plinian airfall Pumice Bonisch Rd. V16/310207	UC702 Murupara-E 1a Rhyolite lava Obsidian Anaputa Pt. V15/244423	UC1137 ho1 1a Rhyolite dome Lava Lk. Rotoiti	UC888 Pre-Matahina 1c Lithic lag breccia Lava Te Weta Rd. V16/300301	UC812 Matahina 1c PDC Dense pumice Lk. Okataina U16/079355
77.07	75.84	77.85	77.48	77.61	76.61	76.60
0.19	0.16	0.11	0.10	0.11	0.16	0.13
12.62	14.62	12.44	12.42	12.50	13.02	13.27
1.48	1.73	1.29	1.29	1.18	1.39	1.37
0.04	0.04	0.04	0.04	0.04	0.05	0.05
0.23	0.17	0.14	0.14	0.07	0.34	0.22
1.07	1.02	0.83	0.83	0.81	1.02	0.89
3.53	2.90	3.52	4.03	4.04	3.33	3.12
3.77	3.52	3.76	3.65	3.62	4.07	4.34
0.01	0.01	0.01	0.01	0.01	0.00	0.01
3.74	4.63	3.94	1.45		3.91	3.23
96.13	95.23	95.93	98.44	98.26	95.97	96.65
1.93	6.18	ND	ND	3.84	10.98	5.74
2.61	4.86	3.93	5.00	4.84	2.96	5.82
16	19	16	16	–	17	17
2	–	1	4	–	6	2
30	41	30	28	–	27	28
115	124	115	117	116	133	140
158	144	106	107	109	121	109
97	100	81	79	77	85	69
19.71	24.14	24.52	24.35	21.60	18.60	22.27
8.45	10.39	8.88	8.59	10.28	9.76	9.36
838	1052	938	934	879	963	788
21.76	23.98	24.50	24.27	23.13	23.69	24.62
46.06	56.24	56.65	56.26	52.70	53.30	54.82
4.17	5.13	5.25	5.08	5.44	4.59	4.80
14.52	17.86	18.50	17.83	18.60	14.72	16.02
2.88	3.84	3.69	3.79	4.06	2.86	3.06
0.63	0.86	0.71	0.73	0.82	0.57	0.53
3.35	4.35	4.11	4.10	4.12	3.21	3.43
0.51	0.67	0.60	0.62	0.69	0.48	0.51
2.91	3.68	3.34	3.50	3.55	2.62	2.92
0.58	0.74	0.64	0.71	0.81	0.56	0.55
1.84	2.36	2.10	2.22	2.90	1.81	1.83
2.04	2.74	2.37	2.44	2.46	2.04	2.18
0.35	0.41	0.38	0.40	0.39	0.34	0.37
4.05	4.77	3.36	3.28	3.16	3.58	3.29
1.64	2.32	1.98	1.73	1.29	1.73	1.89
32.15	36.15	34.17	31.02	30.47	29.53	25.56
13.26	15.45	12.73	13.39	12.89	15.89	17.71
4.36	5.04	4.06	4.88	4.65	5.25	5.83
0.705326			0.705761	0.705766	0.705652	0.705536
0.512688			0.512654	0.512684	0.512672	0.512668

are tholeiitic. The intermediate compositions form broadly coherent trends in major elements with the Group 1 rhyolite (Fig. 8). Some trace elements show more scatter (e.g. Y; Fig. 9) and slight offsets, rather than continuous trends, from Group 2 to Group 1 (Fig. 9). Group 3 basalt are notably lower in Sr and Zr than Groups 1 and 2, but similar in most major and trace elements to similar, fine-grained

juvenile HAB, reported as having mingled with other silicic magmas from the TVZ (Figs. 8, 9).

The light rare-earth elements (LREE) are generally enriched in all groups, but Group 1 rhyolite is more enriched than Groups 2 and 3 (Fig. 10). Middle rare-earth elements (MREE) are depleted in Group 1, but relatively flat in Groups 2 and 3. Group 2 intermediate rocks have

Table 4 continued

UC839 Matahina 3 PDC Pumice Te Weta Rd. V16/300301	UC1100 Matahina 2 PDC Dense pumice Lk. Okataina U16/079355	UC520 Matahina 2 PDC Banded pumice Te Weta Rd. V16/300301	UC501 Matahina 2 PDC Banded pumice Te Weta Rd. V16/300301	UC1121 Matahina 2 PDC Dense pumice Lk. Okataina U16/079355	UC1123 Matahina 2 PDC Dense pumice Lk. Okataina U16/079355	UC832 Matahina 2 PDC Pumice Te Weta Rd. V16/300301
51.29	57.65	58.66	58.90	59.19	63.75	66.33
0.99	1.06	1.08	1.01	0.80	0.75	0.60
18.69	17.55	19.04	18.65	17.33	16.16	17.38
11.85	9.23	9.20	9.15	8.27	6.78	5.80
0.20	0.18	0.16	0.17	0.16	0.12	0.09
5.63	3.67	3.51	3.62	4.28	2.73	1.89
8.88	6.64	4.63	4.69	6.07	4.66	3.02
1.77	2.95	2.48	2.49	2.75	3.07	2.94
0.60	1.02	1.22	1.28	1.12	1.91	1.93
0.09	0.06	0.03	0.05	0.03	0.05	0.02
3.28		4.44	4.48			3.87
96.61	96.36	95.45	95.40	95.86	97.00	95.99
324.69	211.51	212.02	231.41	209.10	189.16	140.32
21.99	13.53	18.01	17.79	34.40	16.26	12.42
21	–	21	21	–	–	19
–	–	–	–	–	–	–
98	–	85	98	–	–	62
18	31	36	39	35	57	57
84	455	367	302	258	238	340
193	320	201	201	224	226	190
30.70	18.76	21.64	24.89	20.43	18.94	20.41
2.65	4.86	5.34	5.58	4.50	6.18	7.73
376	397	343	463	523	556	604
11.74	9.32	11.67	13.17	9.84	13.70	16.05
19.51	19.82	23.05	29.86	22.92	32.52	34.74
4.12	2.67	3.08	3.78	2.84	3.70	3.68
18.29	10.90	12.29	15.51	11.52	13.86	13.39
4.62	2.84	3.00	3.63	2.96	3.22	3.09
1.12	1.12	1.00	1.09	0.99	1.02	0.90
4.43	3.00	3.27	3.69	3.11	3.31	3.15
0.71	0.52	0.54	0.61	0.54	0.53	0.54
4.86	3.03	3.42	3.76	3.22	3.03	3.12
0.90	0.67	0.65	0.75	0.70	0.66	0.57
2.82	2.02	2.08	2.22	2.18	2.10	1.85
2.88	2.14	2.19	2.38	2.27	2.15	2.08
0.44	0.35	0.35	0.38	0.37	0.34	0.35
2.32	8.48	7.55	6.28	4.77	4.50	6.96
0.18	0.34	0.38	0.37	0.32	0.51	0.66
2.76	4.31	5.83	5.75	4.91	8.80	15.31
1.49	3.11	3.91	3.79	3.12	5.31	7.96
0.45	1.23	1.36	1.14	1.29	2.45	2.13
	0.705839					
	0.512659					

Samples are normalized to 100% anhydrous. Major elements given in wt. % and trace elements (ppm)

Trace elements determined by ICP-MS. LOI values are calculated by weight difference. *ND* not detected

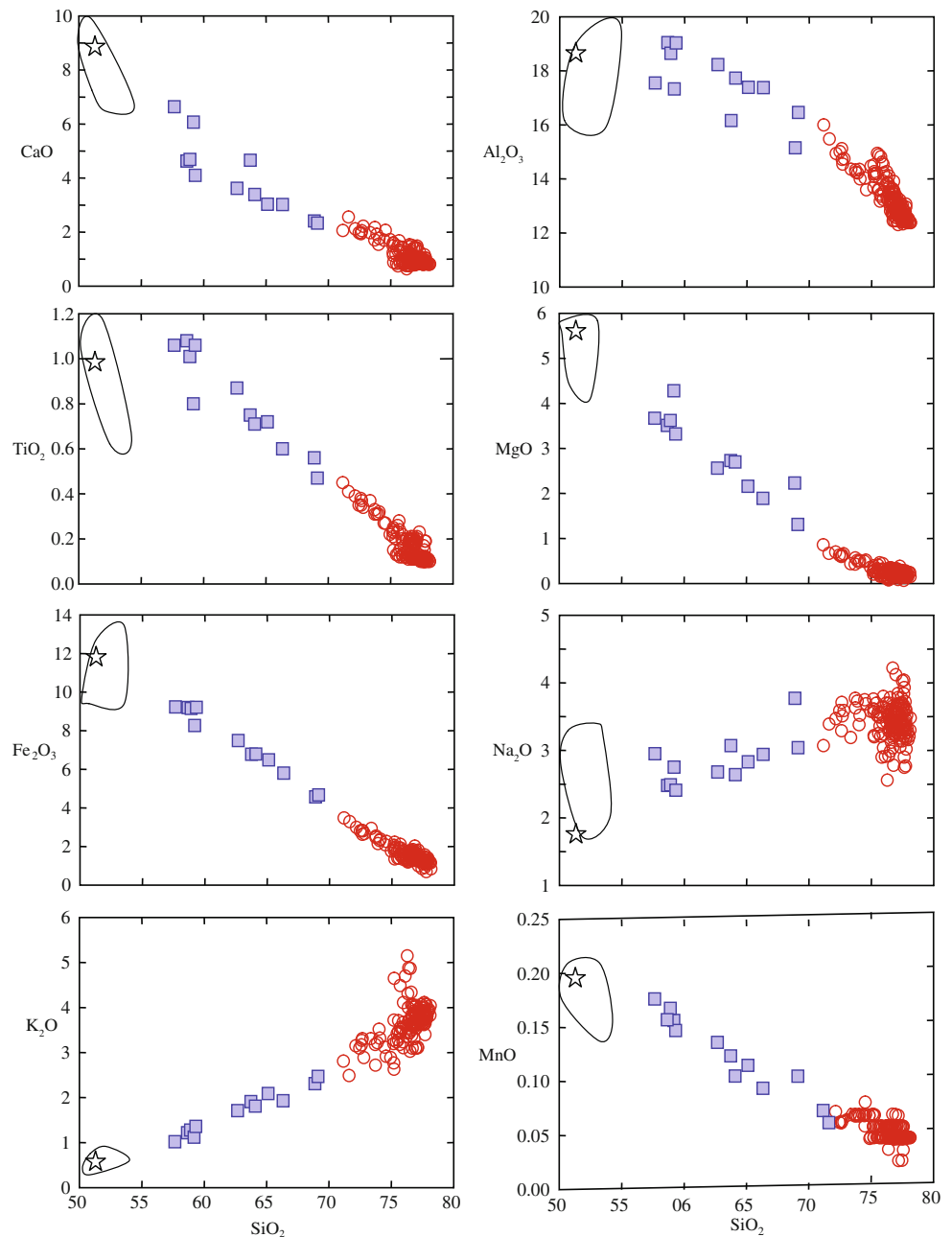
Grid references refer to sample localities on the New Zealand NZMS 1:50,000 maps

either slightly positive or negative Eu anomalies, whereas the Group 1 rhyolite shows deep negative anomalies (Fig. 10).

Group 1 rhyolite displays several distinct and coherent major and trace-element trends, which correlate with the

distinct mineral contents observed in the subgroups outlined above. In general, there are two subparallel trends in most major elements that vary with SiO₂ content (e.g. Fig. 11). Group 1a is defined by low CaO, MgO, Fe₂O_{3T}, TiO₂, and high Al₂O₃ trends and extends to 75.23 wt. %

Fig. 8 Selected major element oxides against silica for the Murupara E–H, Matahina ignimbrite, recycled ignimbrite, and rhyolite lithics (encircled area is high-alumina basalt; data from Gamble et al. 1993)



SiO_2 (e.g. Fig. 11); whereas Group 1b is defined by high CaO, MgO, $\text{Fe}_2\text{O}_{3\text{T}}$, TiO_2 , and low Al_2O_3 trends and extends to the lowest SiO_2 contents (71.16 wt. %; e.g. Fig. 11). Group 1c mostly overlaps with Group 1a but has higher K_2O contents (Fig. 11). The Murupara units E–G and the ‘recycled’ ignimbrite pumice fall geochemically within the Group 1a,b Matahina, but individual pumice tends to share characteristics of both groups or overlap with the two types. The pre-Matahina rhyolite lava dome, exposed along the northern margin of the present day caldera (Fig. 1), is also included in Group 1a.

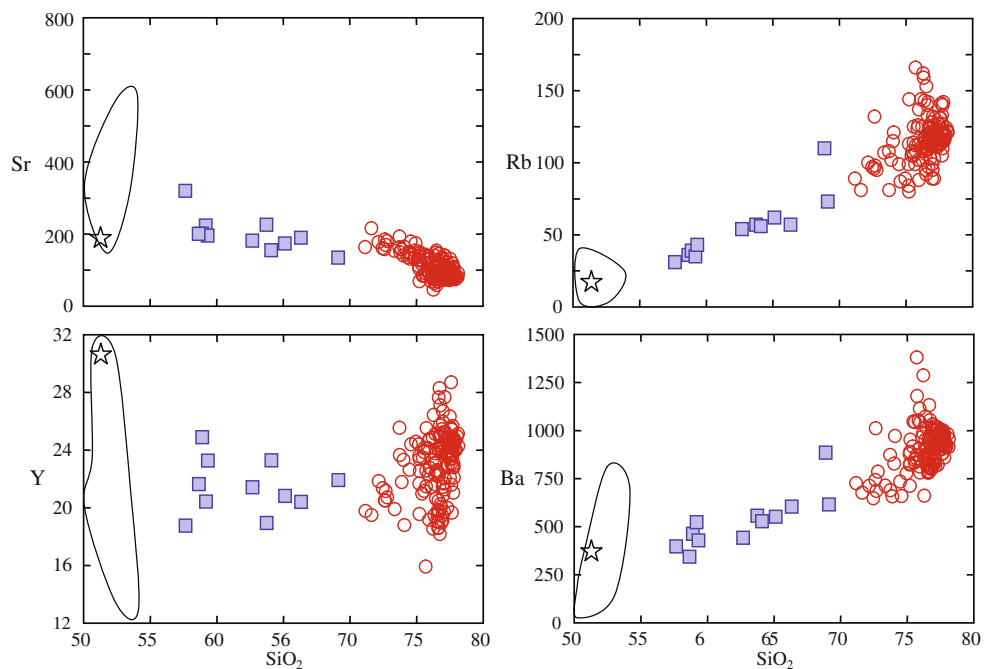
Trace-element variations further define the Group 1 rhyolite. Group 1c has distinctive Rb and Th but falls

within the Group 1a in all other trace-element plots (e.g. Fig. 11). Group 1a has lower Zr, Sr, and Hf than Group 1b but overlaps with Group 1c in Rb, Y, and Th (e.g. Fig. 11). Group 1b has some of the lowest Rb contents but also overlaps with Group 1a,c. Yttrium shows significant scatter among all groups.

Matrix glass

Glass compositions range from 74 to 79 wt. % SiO_2 and mostly overlap with the high-silica rhyolite type. The lowest SiO_2 glass analyzed follows the bulk-rock trend of the Group 1b rhyolite. Although the K_2O content of

Fig. 9 Selected trace elements against silica for the Murupara E–H, Matahina ignimbrite, recycled ignimbrite, and rhyolite lithics. Symbols same as Fig. 8



glass from Group 1c is the highest among the rhyolites, distinct glass compositions also overlap with those from Group 1b (Fig. 12). Group 2 rhyolitic glass compositions overlap with the bulk-rock rhyolite pumice and glass from the rhyolitic pumice (Fig. 12). However, the Group 2 glass compositions diverge slightly from the dominant high- to low-silica glass of the rhyolite. Cl is correlated with indicators of differentiation, and Cl concentrations are generally lowest in the lowest SiO_2 glass analyzed from Group 2 pumice but form a scattered trend to higher contents in the Group 1 pumice (Fig. 13). Some of the biotite-bearing Group 1c pumice also has low Cl contents, but in more evolved glass and may have been affected by partitioning between melt-biotite. Glass in the basalt is unusual and contains the highest Cl contents and low K_2O —this will be addressed below in the discussion.

Sr–Nd isotopes

Strontium and Nd isotopes are broadly within the field of other TVZ rhyolites (Fig. 14a). Pre-Matahina biotite + quartz-bearing rhyolite lithics from the lag breccia and biotite + quartz-bearing pumice from the PDC deposit along the western margin of the caldera (Fig. 1; localities 1 and 2) have Sr–Nd isotope compositions within analytical error of one another (Fig. 14a). The Sr–Nd isotopes of Murupara-E pumice and pre-Matahina rhyolite dome clasts are also within error. Similar to some andesite composite volcanoes outside of the central TVZ, the one most crystalline andesite rock (UC1100) is isotopically similar to

TVZ rhyolite. The isotopic composition of Matahina pumice is slightly negatively correlated with indicators of differentiation (e.g. SiO_2 ; Fig. 14b).

Discussion

Crystal-poor rhyolite from intermediate mush

Many silicic eruptions represent evacuations of a magma system zoned from crystal-poor to crystal-rich (up to 25% crystals) (e.g. Mills et al. 1997). However, few samples that represent intermediate ‘mushes’ (25–55% crystals) have been co-erupted with the voluminous crystal-poor rhyolite (e.g. Hildreth and Fierstein 2000). Marsh (1981) defined a rheological transition at $\sim 25\%$ crystals from a viscous fluid suspension to a high viscosity mush of reticulated crystals. This increase in viscosity had been characterized as a ‘viscosity barrier’ by Smith (1979) preventing efficient extraction; barring energetic disruption—possibly by caldera collapse.

Despite the absence of a copious number of samples representing intermediate crystal ‘mush’ in eruptive deposits, a growing body of evidence indicates that large rhyolitic magma reservoirs evolve via silicic melt extraction from intermediate mushes (see Hildreth 2004; Bachmann and Bergantz 2004; Hildreth and Wilson 2007). Hildreth and Wilson (2007) prefer a model for the well-studied Bishop Tuff ($\sim 600 \text{ km}^3$ rhyolitic magma), whereby secular escape of interstitial melt from a mush would be favoured in extensional environments. Rift

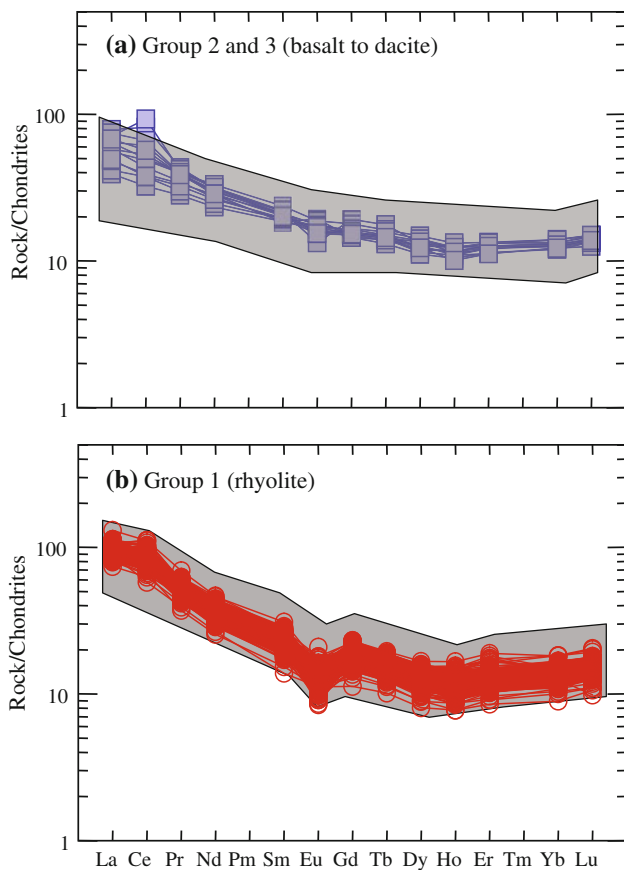


Fig. 10 Field of chondrite-normalized REE patterns for **a** the Groups 2 and 3 basalt to dacite mingled/mixed rocks [Shaded area is representative of mafic to intermediate rocks of two types: (1) high-alumina basalt from monogenetic cinder cones within the central TVZ and andesite from composite volcanoes outside of the central TVZ (data from Gamble et al. 1993; Graham et al. 1995), and **b** the Murupara E–H, Matahina ignimbrite, recycled ignimbrite, and rhyolite lithics [Shaded area represents all TVZ rhyolites (data from Deering et al. 2008)]

related faulting would repeatedly disrupt the mush column, allowing the low viscosity, hydrous rhyolitic melt ($<10^4$ – $10^{5.5}$ Pa s at 700–800°C; Scaillet et al. 1998) to be incrementally extracted.

The following observations are consistent with the melt-rich Matahina rhyolite having been derived from an intermediate crystal mush. First, glass compositions determined for Group 2 intermediate magmas broadly overlap with the *bulk-rock* composition of the Group 1 rhyolite (Fig. 12). This compositional overlap, coupled with the increase in crystallinity from high-silica rhyolite to intermediate rocks, indicates that the intermediate magma represents an accumulation of crystals with a rhyolitic interstitial liquid. This rhyolitic liquid is the Group 1 rhyolite. Second, the Zr contents are much higher in the Group 2 intermediate clasts relative to similar clasts from other TVZ silicic eruptions, indicating zircon accumulation (Fig. 15a). To a lesser extent, a slight positive Eu anomaly

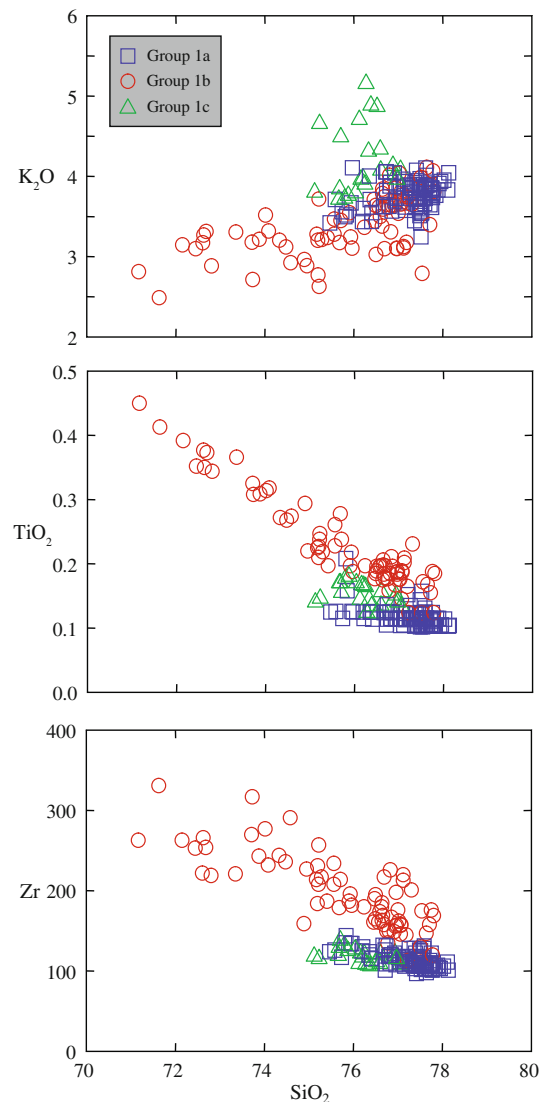


Fig. 11 Selected major and trace elements against silica for rhyolite subgroups also defined by distinct mineral contents

in Group 2 intermediate relative to the Group 3 fine-grained basalt and other TVZ basalts also indicates plagioclase accumulation (Fig. 15b). Third, although scattered, there is a general increase in Cl contents with increasing melt SiO_2 (Fig. 13), which is also reflected in the hornblende chemistry (Fig. 4b) and is consistent with volatile evolution during crystallization (second boiling). Fourth, the intercrystalline continuum of compositions observed in plagioclase, hornblende, orthopyroxene, and oxides (Figs. 3, 4, 5, 6) and normal zoning within individual crystals argues strongly for in situ crystal-melt evolution. A final point is based on pressure, temperature, and oxygen fugacity estimates. They indicate that the Group 2 intermediate magmas resided at greater depths than the Group 1 rhyolite prior to eruption (Table 3), within the mid- to upper-crust at and just below the brittle-

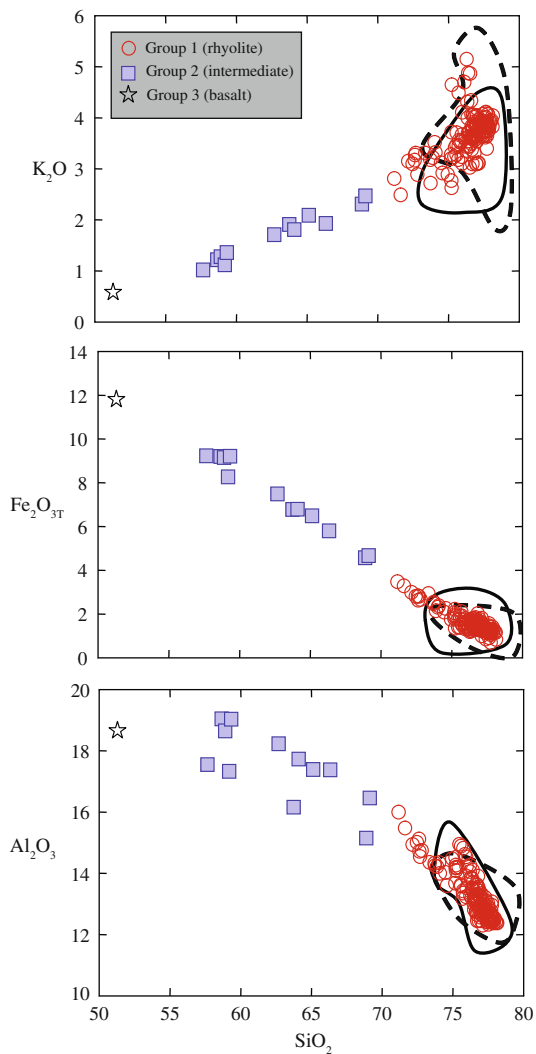


Fig. 12 Glass compositions of selected major element oxides for both intermediate and silicic rocks. Glass analyses are normalized to 100% anhydrous. Open field is Group 1 rhyolite glass, and dashed field is Group 2 intermediate glass

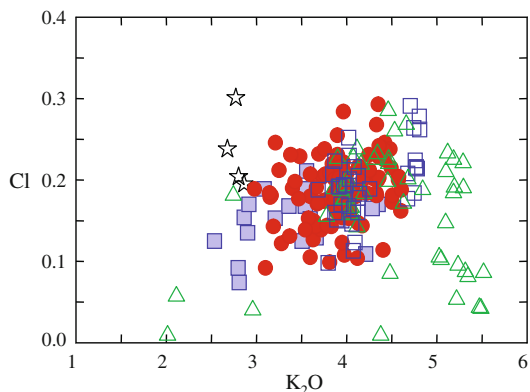


Fig. 13 Cl against K₂O in glass of Groups 1, 2, and 3

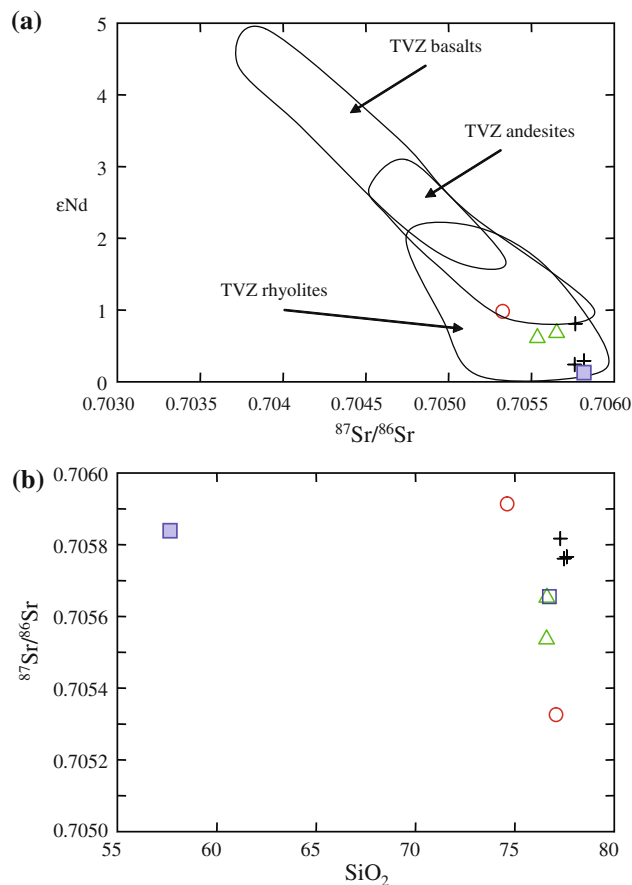


Fig. 14 a ⁸⁷Sr/⁸⁶Sr against εNd values, and b ⁸⁷Sr/⁸⁶Sr against bulk rock SiO₂ for Matahina mafic and felsic compositions. Field for TVZ basalt is from Gamble et al. (1993) and for TVZ andesite from Graham et al. (1995) and references therein. Symbols as in previous figures

ductile transition at 10–12 km (Heise et al. 2007). Estimates of the pre-eruptive magma P–T–fO₂ conditions of the coarse-grained Group 2 are consistent with peak recharge and initial storage temperatures between 950 and 850°C, but detailed analytical traverses of hornblende from core to rim indicate a gradual cooling to near ~800°C just prior to the mingling and mixing with the host Group 1 rhyolite (Deering 2009).

Together, the stratigraphy of compositional types and the temperature and pressure estimates of Group 1 and Group 2 magmas support the existence of only a slight compositional gradient within the crystal-poor cap and a slight thermal gradient from mid- to upper-crust. The order of appearance in the eruptive sequence of the mafic component and the pressure estimates for mafic to felsic magmas allow the construction of a compositional profile from crystal-rich andesite (~50 vol%) with rhyolitic interstitial melt and an abrupt change to a crystal-poor slightly zoned rhyolite.

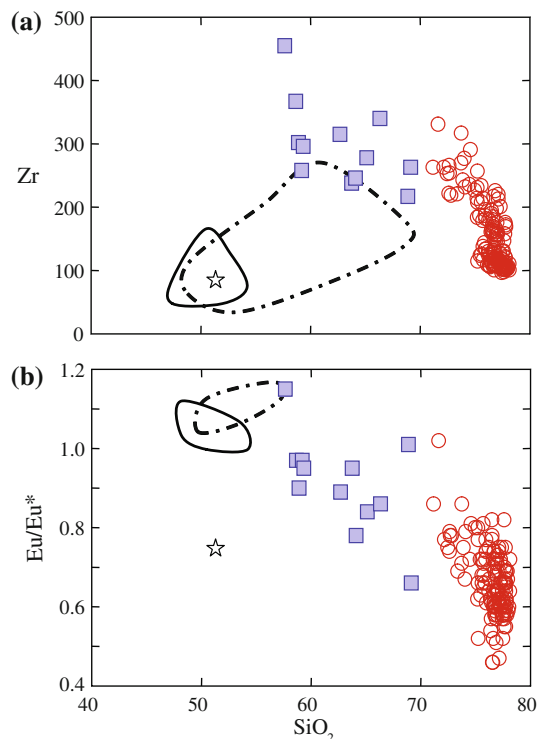


Fig. 15 Zr contents and Eu anomaly (Eu/Eu^*) against silica for all groups, plotted with high-alumina basalt (solid outline: Gamble et al. 1993) and hornblende-bearing quenched mafic clasts (dashed outline: Brown et al. 1998; Wilson et al. 2006). Eu/Eu^* is calculated from the two linear equations $\log_{10}(\text{Sm}_N) = (a \cdot 62) + b$ and $\log_{10}(\text{Tb}_N) = (a \cdot 65) + b$

Compositional gap

The volcanism in the central TVZ is predominantly compositionally bi-modal and consists of volumetrically dominant caldera-forming rhyolitic eruptions and subordinate monogenetic basaltic cone building. This compositional gap has been used to infer that either the rhyolites represent pure metasedimentary crustal melts (which has been rejected based on isotopes; for a review see Graham et al. 1995) or they represent melting of previously emplaced intermediate igneous rocks that never reached the surface. However, mantle-derived melts generated along continental arcs crystallize rapidly upon interaction with the cold crust and follow a wet-oxidizing liquid line of descent (amphibole and oxides), which can drive liquid compositions over the andesite field and instead produce dacite (Grove and Donnelly-Nolan 1986). Therefore, given the presence of amphibole in the intermediate magma and assuming an initial dacite, crystal accumulation and compaction of this magma will produce an andesitic cumulate with a complementary rhyolitic interstitial liquid (Bachmann and Bergantz 2004). A dacitic magma produced in the lower- to middle crust partially fills this compositional

gap and the compositional continuum observed in the minerals preserves a complete liquid line of descent (Figs. 3, 4, 5, 6). Therefore, although the erupted products are compositionally bi-modal, the minerals record the complete series of magma evolution from parental basalt in the lower crust to the rhyolite daughter produced in the mid- to upper-crust.

Origin of rhyolite diversity (groups)

Combined, the geochemical characteristics outlined above are consistent with Group 1 being genetically related to Group 2. However, other features indicate that the conditions of crystallization in the mush column varied slightly: (1) oxygen fugacity ranges from $+0.05$ (ΔNNO) to $+0.49$ (ΔNNO); (2) the hornblende/orthopyroxene ratio ranges from 0.06 to 3.6; and (3) although crystal contents decrease from andesite to dacite, the total crystal contents are different across the range of comparable bulk-rock compositions. Therefore, the range of compositional features and mineral contents of the intermediate magma and geographic separation of the deposits where they are found suggest that the conditions varied slightly across the base of the reservoir and would have produced slightly different rhyolitic liquid compositions. Within this context, we explore, in detail, the origin of the compositional variations of the more evolved Matahina magma(s).

The combination of subparallel geochemical trends and distinct mineral contents and chemistry that define the Group 1 subgroups indicates that each of these melt-rich magmas was produced under slightly different conditions. The correlation between oxygen fugacity and Mg# orthopyroxene and key trace elements supports this inference. For example, Dy (bulk-rock) is quantitatively well correlated with oxygen fugacity and qualitatively with the presence and abundance of hydrous phases consistent with derivation of melt under a range of differing $f\text{O}_2$ and $f\text{H}_2\text{O}$ conditions throughout the magma reservoir (Fig. 16a). The range of $f\text{O}_2$ estimated also correlates well with orthopyroxene Mg# (Fig. 16b), consistent with changes observed in experiments where $f\text{O}_2$ was controlled (e.g. Sisson et al. 2005).

The paucity of disequilibrium textures and apparent equilibrium between melt and orthopyroxene (Fig. 5) in the dominant melt-rich Matahina magma body (Group 1) indicates that mixing may not have played a significant role in generating the compositional diversity (or subgroups) and permits a more comprehensive evaluation of differentiation related to the differences in mineral contents associated with the range of different conditions.

Trace elements are particularly sensitive to fractionation of mineral phases and, therefore, provide a good indicator of magma differentiation. Using the mineral contents and

modal percentages determined by mass balance and point counting, we targeted several trace elements that are preferentially partitioned into hornblende and plagioclase as these are the primary phases that vary in abundance within Group 1 rhyolite. We modeled crystal fractionation extending from rhyodacite compositions, where each has distinct hornblende/plagioclase–orthopyroxene ratios along separate trends. As hornblende and plagioclase are the dominant phases present in the rhyodacites, we chose to model Y and Sr, which are highly partitioned into those phases, to determine the origin of the trace-element variation. Approximately 25% crystal fractionation from a rhyodacite with a hornblende/orthopyroxene ratio varying from high to low produces the range of Group 1b with low to moderate Y contents (Fig. 17) and Group 1a with high Y contents. Group 1c high-silica rhyolite can be produced by ~20% crystal fractionation of the lowest-silica Group 1c rhyolite, generating the observed trends to higher Y values (Fig. 17).

These simple trace-element models show that lateral $f\text{H}_2\text{O}$ and $f\text{O}_2$ variations in the intermediate mush (Group 2) can generate a continuum of compositions (or array) as the hornblende/pyroxene–plagioclase ratio varies (Group 1b,c). A decrease in the amount of dissolved H_2O with decreasing pressure toward the roof of the reservoir might decrease enough for the magma to leave the hornblende stability field and could explain the absence of hornblende in the initial fall deposit (Group 1a). This prediction is consistent with simple calculations using CONFLOW (Mastin 2002) to estimate dissolved H_2O over the vertical thickness (est. 2–3 km) of the crystal-poor portion of the reservoir (5 wt. % to 4 wt. % at the roof). The melt viscosity will also increase, which may trap this bubble-rich layer at the roof.

Magma hybridization

Although P–T constraints and compositional variations can predominantly be explained by crystallization and melt extraction from an andesitic progenitor to produce the rhyolite, mingling/mixing during or slightly before eruption was also an important process and modified the composition of a subordinate volume of the Matahina rhyolite *sensu stricto*. This is supported by the following observations: First, the disequilibrium textures, which are often interpreted to reflect magma mixing, such as deeply embayed plagioclase and overgrowths are found in pumice clasts from the PDC and upper-member deposits. Second, the compositions of some magnetite, hornblende, and glass are bi-modal (not shown in figure), but only in the low-silica rhyolite of the upper ash-flow member and in the PDC deposits. Third, the chemical disequilibrium between pyroxene rim compositions and host melt indicates that the

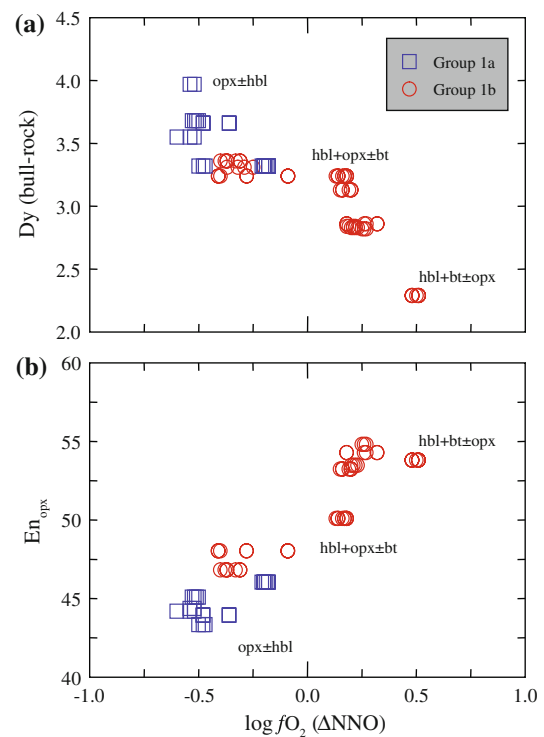


Fig. 16 Log $f\text{O}_2$ (ΔNNO) against orthopyroxene En content and Dy (bulk-rock) illustrates the correlation between type of rhyolite produced via crystal fractionation governed by the oxidation state of the parental melt. Ferromagnesian mineral contents for each rhyolite type are also correlated with the oxidation state of the magma

interstitial melt of the intermediate cumulate mush and the overlying melt-rich rhyolite were slightly different and mineral-melt exchange must have occurred. Fourth, detailed analytical traverses of individual hornblende crystals show a dramatic decrease in temperature along the outer ~150 μm rim, indicating a rapid quenching between the intermediate Group 2 and the cooler rhyolite (Deering 2009). Coupling the distinct bi-modal crystals from some dacite and the low-silica rhyolite implies that, although limited, crystal + melt exchange occurred across the lower extent of the rhyolite magma chamber.

Mafic intrusions

Most arc-generated mantle-derived basalts are wet and will stagnate in the lower crust, crystallizing and assimilating to feed the middle crust with intermediate magma (Carmichael 2002; Tamura and Tatsumi 2002; Dufek and Bergantz 2005; Annen et al. 2006). However, in extensional environments, dike propagation may be favorable allowing some basalt to ascend rapidly. The fine-grained texture and mineral assemblage (hornblende + plagioclase + oxides) of the Group 3 basalt reflects significant undercooling and could be due to direct interaction with the main rhyolitic magma body (e.g. Oruanui eruption; Wilson et al. 2006)

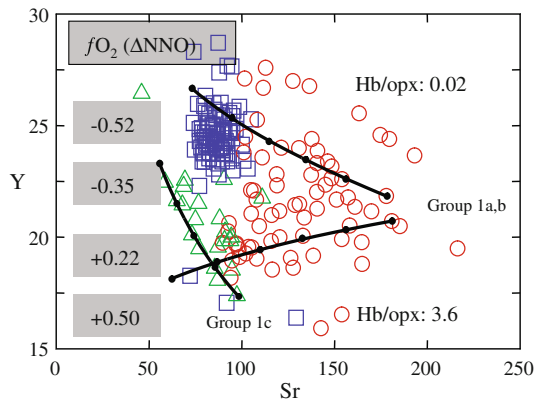


Fig. 17 Trace-element modeling for rhyodacite to high-silica rhyolite for Group A high and low hornblende/orthopyroxene types. Oxygen fugacity is highest for high hornblende/orthopyroxene rhyolite derivatives and lowest for low hornblende/orthopyroxene rhyolite derivatives. Group B modeling trends from the least-evolved to most-evolved biotite + quartz-bearing rhyolite (P_c are from the GERM online database and details of modeling parameters are provided in the online Appendix). Modeling for both Groups A and B is in 5% increments up to 25%. Symbols as in Fig. 11

following penetration of the intermediate mush. The physical process, whereby mafic magma penetrates a more evolved crystalline host mush and spreads out along the floor of a crystal-poor silicic magma chamber, has been observed in exposed upper crustal plutonic sections (Wiebe and Collins 1998; Wiebe et al. 2004). Consequently, we interpret the high Cl contents in the basaltic glass relative to the Group 2 intermediate glass (Fig. 13) as a result of mingling of a volatile-rich, undegassed melt from the basalt with parts of the rhyolitic magma; analogous to mafic sheets preserved in plutons (e.g. Wiebe et al. 2004).

Additionally, if we consider that the amphibole in the basaltic-andesite/andesite recorded several recharge events during the mush evolution (Deering 2009), perhaps these recharge events were coincident with basalt-rhyolite interaction and triggering of earlier Murupara events. Basaltic triggering of smaller rhyolitic eruptions in Okataina has been documented for more recent volcanic activity (e.g. Leonard et al. 2002; Shane et al. 2007), and monogenic basalt eruptions are closely temporally associated with other rhyolitic eruptions (e.g. Schmitz and Smith 2004).

Eruptive model

Pre-Matahina volcanism/magmatism

The bulk-rock compositions, mineral compositional overlap, and isotopic similarities among the Murupara E, F, and G units, pre-Matahina rhyolite domes, Group 1c lithics, and the Group 1 Matahina rhyolite provide some temporal constraints on the assembly of Matahina magmas prior to

the catastrophic event. Extrusive dome construction prior to the Matahina eruption apparently extended out to the north and northeastern caldera boundaries and is probably similar to the spatial extent of the dome complex constructed over the last ~26 kyrs. within the OVC. Although the glass compositions and some bulk rock compositions of biotite-bearing rhyolite pumice from the syn-collapse PDC deposit on the west of the caldera (Fig. 1; locality 1) are similar, the higher K_2O indicates they may be a distinct magma batch.

The eruptive activity that preceded the Matahina eruption signified the early stages of magma assembly and indicates that the magma varied slightly in composition and mineral assemblage within the trace of the caldera. A schematic of the pre/syn-eruptive magmatic system beneath the OVC is provided in Fig. 18. Periodic venting of the Group 1c biotite-bearing, Group 1b orthopyroxene + hornblende-bearing, and Group 1a orthopyroxene ± hornblende-bearing magma types occurred prior to the climactic Matahina eruption. The frequency, style, and volume could be compared to the current activity within the OVC, which has erupted smaller volumes of rhyolite that are distinctly different along the two linear vent zones (Nairn 2002). Distribution of these magmas within the current trace of the caldera complex and the timing of the Group 1c biotite-bearing rhyolite dome building remain unclear, but the exposures of the Group 1a,b rhyolite dome remnants (Fig. 1; localities 8 & 9) are consistent with the existence of a magma reservoir that extended to the north and northeastern caldera margins.

Matahina eruption

The early plinian phase of the Matahina eruption only evacuated Group 1a, high-silica rhyolite, which contains rare hornblende only at the top of the fall deposit. Although the Group 1b rhyolite appears in the first flow deposit, the low-silica, Group 1b was only found to the southeast in one pinkish ash-flow deposit, which was considered the upper ash-flow member of the Matahina by Bailey and Carr (1994). Therefore, the distribution of the final phase of the eruption appears to be primarily along an array from east/southeast to west and includes not only the Group 1a,b rhyolitic magma types but also the Group 1c rhyolite and Groups 2 and 3 from the PDC deposits. Importantly, the Group 1a rhyolite is still mixed within the PDC deposit. Consequently, we infer that the collapse corresponded with unzipping of the crust along ring faults tapping the uppermost portion of the magma reservoir unevenly through time. A similar model was proposed for caldera collapse-induced late-stage mixing and exhumation of mafic mush along the Ossipee ring dyke, New Hampshire, USA (Kennedy and Stix 2007). The

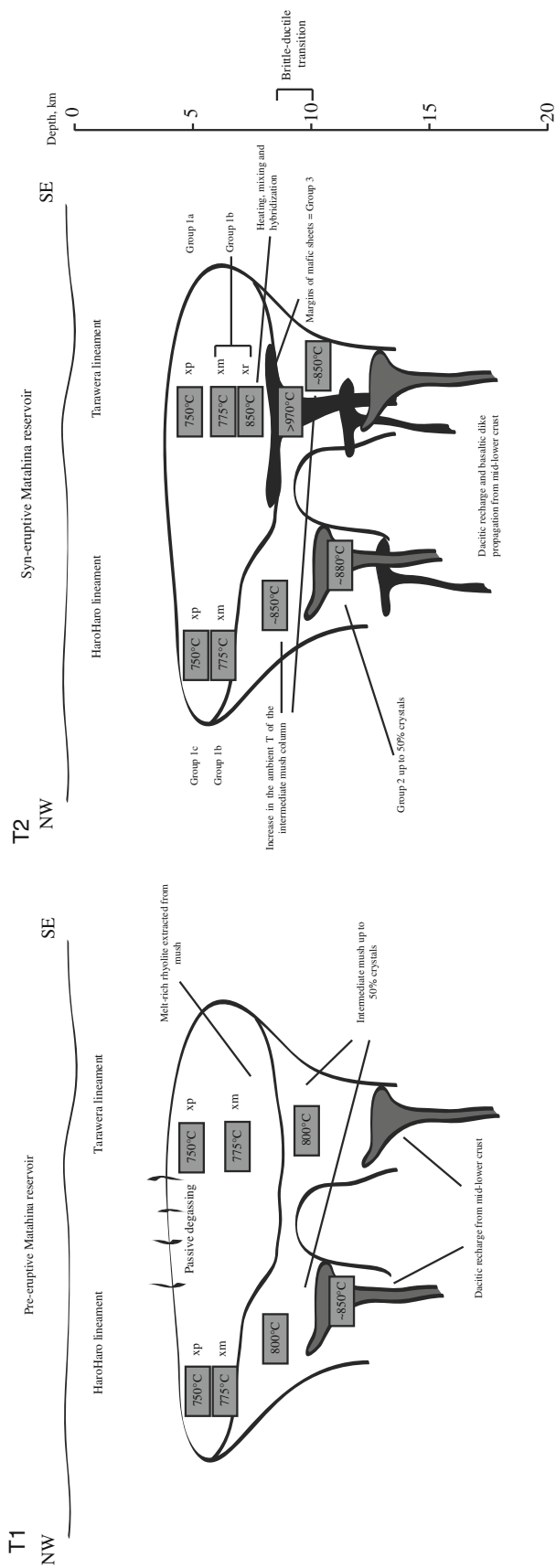
Fig. 18 Schematic cross-section from NW-SE through the OVC, illustrating the magmatic plumbing system prior to and during the Matahina eruption. Intruded basalts are sandwiched between crustal greywacke and intermediate intrusives between 15 and 30 km depth. The compositional and thermal gradient includes the amphibole-bearing cumulate and crystal-rich intermediate magmas up to the brittle-ductile transition at ~8 km depth, whereas the rhyolitic magma reservoirs develop between 4 and 8 km depth. *Upper crust*: A1,2 = Group A rhyolites and B = Group B rhyolite. *Middle crust*: A = Group A andesite–dacite and B = Group B andesite–dacite

exhumation of the coarse-grained intermediate mush likely represents mid- to upper-crustal aliquots, which are squeezed out along ring faults as the crust founders. Late-stage assimilation of the foundering crust is also evidenced by the slight increase in Sr–Nd isotopes from the dominant melt-rich rhyolite to subordinate, crystal-rich andesite magma (Fig. 14).

The eruption of more than one, compositionally distinct, rhyolitic magma is not unique in the TVZ. Other eruptions have also had several compositionally distinct magma bodies erupt that could be related by crystal fractionation (e.g. Whakamaru (Brown et al. 1998) and Rotoiti (Schmitz and Smith et al. 2004)). Even the eruption of two distinct mafic magma types is not unique as Wilson et al. (2006) showed both a calc-alkaline and tholeiitic type interacted with the Oruanui rhyolitic magma. What is unique is the crystal content (phenocrystic hornblende) and abundance within the mafic clasts, which represent a crystal mush zone within the mid- to upper-crust that has rarely been sampled.

Conclusions

1. Crystal accumulation and melt extraction are the dominant processes involved in producing the melt-rich Matahina rhyolite and likely applies to the petrogenesis of all TVZ rhyolites.
2. The intermediate cumulate mush partially fills the compositional gap observed in the TVZ (dacite compositions), but a wet liquid line of descent predicts that a small gap between basalt and dacite may still be a natural consequence of arc-related magmatism.
3. Rhyolitic compositional diversity (groups) can be explained by lateral or vertical variations in fluid content, which in turn influences the proportion of hornblende/plagioclase–pyroxene and ultimately generates a range of compositions. Although likely only a temporary feature of the crystal-poor rhyolite reservoir, the exsolved bubble gradient and inherent difference in viscosity that arises may trap melt at the roof and give rise to a distinct ‘batch’ of melt-rich magma.



4. Mixing was only important in influencing the composition of subordinate aliquots of the main Matahina rhyolite magma body, modifying the rhyolite composition near the mush-melt interface in the late stages of the eruption and were probably induced by the caldera collapse.
5. This case study of the Matahina eruption may provide our first insight into the deeper crustal processes that drive production of the highest volumes of rhyolite erupted on earth over the past two million years.

Acknowledgments Financial support for this study was generously provided by the Royal Society of New Zealand, Marsden Fund (UOC0508) and the Department of Geological Sciences, University of Canterbury, Mason Trust Fund. Electron microprobe analysis at the University of Michigan was supported by NSF grant #EAR-9911352. Rose Turnbull from the University of Canterbury and Joel Baker and Monica Handler at Victoria University are thanked for preparation and analysis of samples for Sr–Nd isotopes.

References

- Annen C, Blundy JD, Sparks RSJ (2006) The genesis of intermediate and silicic magmas in deep crustal hot zones. *J Petrol* 47:505–539
- Bachmann O, Bergantz GW (2004) On the origin of crystal-poor Rhyolites: extracted from batholithic crystal mushes. *J Petrol* 45:1565–1582
- Bacon CR, Druitt TH (1988) Compositional evolution of the zoned calcalkaline magma chamber of Mount Mazama, Crater Lake, Oregon. *Contrib Mineral Petrol* 98:224–256
- Bacon CR, Hirschmann MM (1988) Mg/Mn partitioning as a test for equilibrium between coexisting Fe–Ti oxides. *Am Mineral* 73:57–61
- Bailey RA, Carr RG (1994) Physical geology and eruptive history of the Matahina Ignimbrite, Taupo Volcanic Zone, North Island, New Zealand. *N Z J Geol Geophys* 37:319–344
- Beresford SW (1997) Volcanology and Geochemistry of the Kaingaroa Ignimbrite, Taupo Volcanic Zone, New Zealand. Unpublished PhD thesis, University of Canterbury Library
- Blundy J, Cashman K (2001) Ascent-driven crystallisation of dacite magmas at Mount St. Helens, 1980–1986. *Contrib Mineral Petrol* 140:631–650
- Brown SJA, Wilson CJN, Cole JW, Wooden JL (1998) The Whakamaru Group ignimbrites, Taupo volcanic zone, New Zealand: evidence for reverse tapping of a zoned silicic magmatic system. *J Volcanol Geotherm Res* 84:1–37
- Carmichael ISE (2002) The andesite aqueduct: perspectives on the evolution of intermediate magmatism in west-central (105–99 degrees W) Mexico. *Contrib Mineral Petrol* 143(6):641–663
- Clemens JD (2003) S-type granite-petrogenetic issues, models and evidence. *Earth-Sci Rev* 61:1–18
- Clemens JD, Wall VJ (1984) Origin and evolution of a peraluminous ignimbrite suite: the Violet Town Volcanics. *Contrib Mineral Petrol* 88:354–371
- Cole JW, Spinks KD, Deering CD, Nairn IA, Leonard GS (2010) Volcanic and structural evolution of the Okataina Volcanic Centre; dominantly silicic volcanism associated with the Taupo Rift, New Zealand. *J Volcanol Geotherm Res* 190:123–135
- Deering CD (2009) Cannibalization of an amphibole-rich andesitic progenitor induced by caldera-collapse during the Matahina eruption: evidence from amphibole compositions. *Am Mineral* 94:1162–1174
- Deering CD, Cole JW, Vogel TA (2008) A rhyolite compositional continuum governed by lower crustal source conditions in the Taupo volcanic zone, New Zealand. *J Petrol* 49:2245–2276
- Dufek J, Bergantz GW (2005) Lower crustal magma genesis and preservation; a stochastic framework for the evaluation of basalt-crust interaction. *J Petrol* 46:2167–2195
- Féménias O, Mercier J-CC, Nkono C, Diot H, Berza T, Tatu M, Demaiffe D (2006) Calcic-amphibole growth and compositions in calc-alkaline magmas: evidence from the Motru Dike Swarm (Southern Carpathians, Romania). *Am Mineral* 91:73–81
- Gamble JA, Smith IEM, McCulloch MT, Graham IJ, Kokelaar BP (1993) The geochemistry and petrogenesis of basalts from the Taupo Volcanic Zone and Kermadec Island Arc. *S.W. Pacific. J Volcanol Geotherm Res* 54:265–290
- Ghiorso MS, Evans BW (2008) Thermodynamics of rhombohedral oxide solid solutions and a revision of the Fe–Ti two-oxide geothermometer and oxygen-barometer. *Am J Sci* 308:957–1039
- Ghiorso MS, Sack RO (1991) Fe–Ti oxide geothermometry: thermodynamic formulation and estimation of intensive variables in silicic magmas. *Contrib Mineral Petrol* 108:485–510
- Graham IJ, Gulson BL, Hedenquist JW, Mizon K (1992) Petrogenesis of late Cenozoic volcanic rocks from the Taupo volcanic zone, New Zealand, in the light of new lead isotope data. *Geochim Cosmochim Acta* 56:2797–2819
- Graham IJ, Cole JW, Briggs RM, Gamble JA, Smith IEM (1995) Petrology and petrogenesis of volcanic rocks from the Taupo Volcanic Zone: a review. *J Volcanol Geotherm Res* 68:59–87
- Grove TL, Donnelly-Nolan JM (1986) The evolution of young silicic lavas at Medicine Lake Volcano, California: implications for the origin of compositional gaps in calc-alkaline series lavas. *Contributions to Mineralogy and Petrology* 92: 281–302
- Healy J (1962) Structure and volcanism in the Taupo volcanic zone, New Zealand. *Geophys Monogr* 6:151–157
- Heise W, Bibby HM, Grant CT, Bannister SC, Ogawa Y, Takakura S, Uchida T (2007) Melt distribution beneath a young continental rift; the Taupo Volcanic Zone, New Zealand. *Geophys Res Lett* 34:28
- Hildreth W (2004) Volcanological perspectives on Long Valley, Mammoth Mountain, and Mono Craters: several contiguous but discrete systems. *J Volcanol Geotherm Res* 136(3–4):169–198
- Hildreth W, Fierstein J (2000) Katmai volcanic cluster and the great eruption of 1912. *Geol Soc Am Bull* 112:1594–1620
- Hildreth W, Wilson CJN (2007) Compositional zoning of the Bishop Tuff. *J Petrol* 48:951–999
- Hildreth W, Halliday AN, Christiansen RL (1991) Isotopic and chemical evidence concerning the genesis and contamination of basaltic and rhyolitic magma beneath Yellowstone Plateau volcanic field. *J Petrol* 32:63–137
- Housh TB, Luhr JF (1991) Plagioclase-melt equilibria in hydrous systems. *Am Mineral* 76:477–492
- Johannes W, Holtz F (1990) Formation and composition of H₂O undersaturated granitic melts. In: Ashworth JR, Brown M (eds) High-temperature metamorphism and crustal anatexis. Unwin Hyman, London, pp 87–104
- Kennedy B, Stix J (2007) Magmatic processes associated with caldera collapse at Ossipee ring dyke, New Hampshire. *Geol Soc Am Bull* 119:3–17
- Leake BE, Wooley AR, Arps CES, Birch WD, Gilbert MC, Grice JD, Hawthorne FC, Kato A, Kisch HJ, Krivovichev VG, Linthout K, Laird J, Mandarino JA, Maresch WV, Nickel EH, Rock NMS, Schumacher JC, Smith DC, Stephensen NCN, Ungaretti L, Whittaker EJW, Youzhi G (1997) Nomenclature of amphiboles:

- report of the Subcommittee on Amphiboles of the International Mineralogical Association, Commission on New Minerals and Mineral Names. *Am Mineral* 82:1019–1037
- Leonard GS, Begg J (2010) Geology of the Rotorua area: scale. 1:250,000. Lower Hutt: Institute of Geological & Nuclear Sciences. Institute of Geological & Nuclear Sciences 1:250,000 geological map 5. + 1 folded map
- Leonard GS, Cole JW, Nairn IA, Self S (2002) Basalt triggering of the c. AD 1305 Kaharoa rhyolite eruption, Tarawera Volcanic Complex, New Zealand. *J Volcanol Geotherm Res* 115:461–486
- Leonard GS, Calvert AT, Wilson CJN, Gravley DM, Deering CD (2008) Coastal uplift linked to sea level changes and a record of early Rotorua-Okataina eruptions: constraints from new Taupo Volcanic Zone ^{40}Ar - ^{39}Ar geochronology, New Zealand. International Association of Volcanology and Geochemistry of Earth's Interior, Iceland
- Manning DA (1995) Late Pleistocene tephrostratigraphy of the Eastern Bay of Plenty region, New Zealand. Unpublished PhD thesis, Victoria University
- Manning DA (1996) Middle-late Pleistocene Tephrostratigraphy of the Eastern Bay of Plenty, New Zealand. *Q Int* 34–36:3–12
- Marsh BD (1981) On the crystallinity, probability of occurrence, and rheology of lava and magma. *Contrib Mineral Petrol* 78:85–98
- Mastin L (2002) Insights into volcanic conduit flow from an open-source numerical model. *Geochem Geophys Geosyst* 3. doi: [10.1029/2001GC000192](https://doi.org/10.1029/2001GC000192)
- McCulloch MT, Kyser TK, Woodhead JD, Kinsley L (1994) Pb-Sr-Nd-O isotopic constraints on the origin of rhyolites from the Taupo volcanic zone of New Zealand; evidence for assimilation followed by fractionation from basalt. *Contrib Mineral Petrol* 115:303–312
- Mills JG, Saltoun BW, Vogel TA (1997) Magma batches in the Timber Mountain magmatic system Southwestern Nevada Volcanic Field, Nevada, USA. *J Volcanol Geotherm Res* 78:185–208
- Milner DM, Cole JW, Wood CP (2001) Mamaku Ignimbrite: a caldera-forming ignimbrite erupted from a compositionally zoned magma chamber in Taupo Volcanic Zone, New Zealand. *J Volcanol Geotherm Res* 122:243–264
- Nairn IA (2002) Geology of the Okataina Volcanic Centre, scale 1:50 000. Institute of Geological & Nuclear Sciences geological map 25. 1 sheet + 156 p. Lower Hutt: Institute of Geological & Nuclear Sciences: 20
- Pichavant M, Kontak DJ, Briquieu L, Herrera JV, Clark AH (1988a) The Miocene-Pliocene Macusani Volcanics, SE Peru, 1. Mineralogy and magmatic evolution of a two-mica aluminosilicate-bearing ignimbrite suite. *Contrib Mineral Petrol* 100:300–324
- Pichavant M, Kontak DJ, Briquieu L, Herrera JV, Clark AH (1988b) The Miocene-Pliocene Macusani Volcanics, SE Peru, 2. Geochemistry and origin of felsic peraluminous magma. *Contrib Mineral Petrol* 100:325–338
- Riley TR, Leat PT, Pankhurst RJ, Harris C (2001) Origins of large volume rhyolitic volcanism in the Antarctic Peninsula and Patagonia by crustal melting. *J Petrol* 42:1043–1065
- Scaillet B, Holtz F, Pichavant M (1998) Phase equilibrium constraints on the viscosity of silicic magmas; 1, volcanic-plutonic comparison. *J Geophys Res B, Solid Earth Planets* 103(11): 27,257–27,266
- Schmidt MW (1992) Amphibole composition in tonalite as a function of pressure; an experimental calibration of the Al-in-hornblende barometer. *Contrib Mineral Petrol* 110:304–310
- Schmitz MD, Smith IEM (2004) The petrology of the Rotoiti eruption sequence, Taupo volcanic Zone: an example of fractionation and mixing in a rhyolitic system. *J Petrol* 45:2045–2066
- Shane P, Martin SB, Smith VC, Beggs KF, Darragh MB, Cole JW, Nairn IA (2007) Multiple rhyolite magmas and basalt injection in the 17.7 ka Rerewhakaaitu eruption episode from Tarawera volcanic complex, New Zealand. *J Volcanol Geotherm Res* 164:1–26
- Sisson TW, Bacon CR (1999) Gas-driven filter pressing in magmas. *Geology* 27:613–616
- Sisson TW, Ratajeski K, Hankins WB, Glazner AF (2005) Voluminous granitic magmas from common basaltic sources. *Contrib Mineral Petrol* 148:542–565
- Smith RL (1979) Ash-flow magmatism. *Geological Society of America. Special Paper* 180: 5–27
- Smith IEM, Stewart RB, Price RC (2003) The petrology of a large intra-oceanic silicic eruption: the Sandy Bay Tephra, Kermadec Arc, Southwest Pacific. *J Volcanol Geotherm Res* 124:173–194
- Tamura Y, Tatsumi Y (2002) Remelting of an andesitic crust as a possible origin for rhyolitic magma in oceanic arcs: an example from the Izu-Bonin arc. *J Petrol* 43(6):1029–1047
- Ulfbeck D, Baker J, Waight T, Krogstad E (2003) Rapid sample digestion and chemical separation of Hf for isotopic analysis by MC-ICPMS. *Talanta* 59:365–373
- Vogel TA, Flood TP, Patino LC, Wilmot MS, Maximo RPR, Arpa CB, Arcilla CA, Stimac JA (2006) Geochemistry of silicic magmas in the Macolod Corridor, SW Luzon, Philippines: evidence of distinct, mantle-derived, crustal sources for silicic magmas. *Contrib Mineral Petrol* 151:267–281
- Waight TE, Baker JA, Peate DW (2002) Sr isotope ratio measurements by double-focusing MC-ICPMS: techniques, observations and pitfalls. *Int J Mass Spectrom* 221:229–244
- Wiebe RA, Collins WJ (1998) Depositional features and stratigraphic sections in granitic plutons: implications for the emplacement and crystallization of granitic magma. *J Struct Geol* 20:1273–1289
- Wiebe RA, Manon MR, Hawkins DP, McDonough WF (2004) Late-stage mafic injection and thermal rejuvenation of the Vinalhaven granite, Coastal Maine. *J Petrol* 45:2133–2153
- Wilson CJN, Rogan AM, Smith IEM, Northey DJ, Nairn IA, Houghton BF (1984) Caldera volcanoes of the Taupo volcanic zone, New Zealand. *J Geophys Res* 89:8463–8484
- Wilson CJN, Houghton BF, McWilliams MO, Lanphere MA, Weaver SD, Briggs RM (1995) Volcanic and structural evolution of Taupo volcanic zone, New Zealand: a review. *J Volcanol Geotherm Res* 68:1–28
- Wilson CJN, Blake S, Charlier BLA, Sutton AN (2006) The 26.5 ka Oruanui Eruption, Taupo Volcano, New Zealand: development, characteristics and evacuation of a large Rhyolitic magma body. *J Petrol* 27:35–69